

SYSTEMATIC SURVEY FOR [O II], [O III], AND H α BLOBS AT $z = 0.1 - 1.5$: THE IMPLICATION FOR EVOLUTION OF GALACTIC-SCALE OUTFLOW

SURAPHONG YUMA¹, MASAMI OUCHI², ALYSSA B. DRAKE³, SEIJI FUJIMOTO^{2,4}, TAKASHI KOJIMA^{2,5}, AND YUMA SUGAHARA^{2,5}

¹Department of Physics, Faculty of Science, Mahidol University, Bangkok 10400, Thailand; suraphong.yum@mahidol.ac.th

²Institute for Cosmic Ray Research, The University of Tokyo, Kashiwa-no-ha, Kashiwa 277-8582, Japan

³CRAL, Observatoire de Lyon, Université Lyon 1, 9 avenue Charles André, 69561 Saint Genes Laval Cedex, France

⁴Department of Astronomy, University of Tokyo, Hongo, Bunkyo-ku, Tokyo 113-0033, Japan and

⁵Department of Physics, University of Tokyo, Hongo, Bunkyo-ku, Tokyo 113-0033, Japan

Accepted for publication in *ApJ*

ABSTRACT

We conduct a systematic search for galaxies at $z = 0.1 - 1.5$ with [O II] λ 3727, [O III] λ 5007, or H α λ 6563 emission lines extended over at least 30 kpc by using deep narrowband and broadband imaging in Subaru-XMM Deep Survey (SXDS) field. These extended emission-line galaxies are dubbed [O II], [O III], or H α blobs. Based on a new selection method that securely select extended emission-line galaxies, we find 77 blobs at $z = 0.40 - 1.46$ with the isophotal area of emission lines down to $1.2 \times 10^{-18} \text{ erg s}^{-1} \text{ cm}^{-2} \text{ kpc}^{-2}$. Four of them are spectroscopically confirmed to be [O III] blobs at $z = 0.83$. We identify AGN activities in 8 blobs with X-ray and radio data, and find that the fraction of AGN contribution increases with increasing isophotal area of the extended emission. With the Kolmogorov-Smirnov (KS) and Anderson-Darling tests, we confirm that the stellar-mass distributions of H α and [O II] blobs are not drawn from those of the emitters at the $> 90\%$ confidence level in that H α and [O II] blobs are located at the massive end of the distributions, but cannot reject null hypothesis of being the same distributions in terms of the specific star formation rates. It is suggested that galactic-scale outflows tend to be more prominent in more massive star-forming galaxies. Exploiting our sample homogeneously selected over the large area, we derive the number densities of blobs at each epoch. The number densities of blobs decrease drastically with redshifts at the rate that is larger than that of the decrease of cosmic star formation densities.

Keywords: galaxies: high redshift — galaxies: evolution — galaxies: formation

1. INTRODUCTION

It has long been known that galaxies in the local universe can be divided into categories according to the so-called Hubble sequence. Main populations are spiral/disk galaxies with active star-forming activity and elliptical galaxies that rarely form new stars and evolve passively. Astronomers suggested that progenitors of elliptical galaxies should somehow stop forming new stars and start evolving passively at some epoch around $z \sim 1$ (e.g., Trujillo & Aguerri 2004; McIntosh et al. 2005). The cessation of star formation in galaxies occurs when gas in those galaxies is used up and/or galactic-scale outflow mechanism expels cool gas out of galaxies at the rate larger than the accretion of inflowing gas (e.g., Lilly et al. 2013). Feedback from active galactic nuclei (AGN) and supernova explosions has been introduced to explain the gas outflow and subsequently the suppression of star formation. It is a key process in turning star-forming galaxies into passively evolving massive ellipticals. In a theoretical framework, strong radiation from an accretion disk and radio jet of an AGN at the center of a galaxy prevents a cooling flow of gas, leading to star-formation quenching in massive galaxies at the massive end of the stellar mass function (e.g., Somerville et al. 2008). On the other hand, supernova and stellar winds heat up cold gas in the interstellar medium (ISM) that is expelled by outflow and suspends the star formation in low-mass galaxies (e.g., Benson et al. 2003).

To date, outflows have been extensively studied in various types of galaxies; e.g., Ultra Luminous Infrared Galaxies (ULIRGs, Heckman et al. 1990; Martin 2005; Soto et al. 2012), Sub-Millimeter Galaxies (SMGs, Alexander et al. 2010), and star-forming galaxies (Steidel et al. 2010; Mar-

tin et al. 2012; Kornei et al. 2012; Erb et al. 2012; Bradshaw et al. 2013). Recently, Cheung et al. (2016) studied the outflow in AGN hosting quiescent galaxies and showed that an active SMBH even in low-luminosity AGNs can provide sufficient energy to drive the outflow. However, study of gas outflow at a large scale, which is closely related to the quenching process of star formation and subsequently to the evolution of elliptical galaxies, is still incomplete, especially for non-AGN galaxies.

The large-scale outflow of gas takes place in a relatively short timescale; therefore, it is difficult for observations to pinpoint a galaxy in the middle of such a major process that subsequently stops star-forming activity. Yuma et al. (2013, hereafter Y13) introduced the first systematic search for galaxies with spatially extended [O II] λ λ 3726, 3729 emission (dubbed “[O II] blobs” or “O IIBs”). The idea of their method is to select the galaxies with the strong [O II] emission line that is redshifted and falls into the narrowband filter and examine the spatial extension of the [O II] emission line from the narrowband image after subtracting contribution of the stellar continuum. With deep narrowband imaging covering a survey volume of $1.9 \times 10^5 \text{ Mpc}^3$ in the Subaru XMM Deep Survey (SXDS), Y13 discovered a giant [O II] blob, named O IIB1, with a spatial extent of [O II] emission over 75 kpc and identified a total of 12 O IIBs with > 30 -kpc extension at $z \sim 1.2$. O IIB1 is identified as an AGN with the 6σ detection of the high-excitation [Ne V] λ 3426 emission line, while the others are star-forming galaxies with no AGN activity. According to the surface brightness profiles, the oxygen emission of these O IIBs is extended beyond the stellar component and is thought to be due to hot metal-rich

gas outflowing from galaxies rather than pristine gas inflowing from metal-poor intergalactic medium (IGM; e.g., [Aguirre et al. 2008](#); [Fumagalli et al. 2011](#)). The outflow hypothesis is confirmed by the spectroscopic analysis of three O II B1 (Y13; [Harikane et al. 2014](#)). The spectrum of O II B1 with the largest extent of [O II] emission line show the blueshifted Fe II $\lambda 2587$ absorption and Fe II $\lambda 2613$ emission lines with the outflow velocities of $500 - 600 \text{ km s}^{-1}$. The outflow in the other two O II B1s is examined from the blueshifted Mg II $\lambda 2796, 2804$ and Fe II $\lambda 2587$ absorption lines. The derived outflow velocities range from 80 km s^{-1} to 260 km s^{-1} , which is consistent with those of normal star-forming galaxies. Furthermore, [Harikane et al. \(2014\)](#) used line ratios to examine the energy source of another O II B1 at $z \sim 1.2$ by using the blue diagram ([O III]/H β versus [O II]/H β ; [Lamareille et al. 2004](#); [Lamareille 2010](#)) and found that the outflow is powered by both star formation and the AGN. Searching for galaxies with extended oxygen emission lines provides a systematic sample of galaxies showing metal-rich large-scale outflow both with and without AGNs. Although extended oxygen emission is already seen in some AGNs (e.g., [Nesvadba et al. 2008](#)), this method efficiently provides samples of large-scale outflows in non-AGN galaxies for the first time.

As a systematic search, Y13 are able to determine the number density of the O II B1s at $z \sim 1.2$. It is $\sim 5 \times 10^{-6} \text{ Mpc}^{-3}$ for O II B1-type giant blobs with an AGN. The number density is comparable to that of the AGNs with outflow at the similar redshift ([Barger et al. 2005](#); [Barger & Cowie 2005](#)). The number density of all O II B1s at $z \sim 1.2$ including O II B1 is $6.3 \times 10^{-5} \text{ Mpc}^{-3}$. By comparing the O II B1 number density with those of star-forming galaxies at the similar redshift, it is implied that 3% of star-forming galaxies at $z \sim 1$ are quenching the star formation through an outflow involving extended [O II] emission.

Although this method is successful in systematically selecting galaxies with large-scale outflows by using only the imaging data, Y13 only focused their study at one specific epoch of the universe, i.e., at $z \sim 1.2$. In order to understand the wider picture of gas outflow, AGN/stellar feedback, and eventually the galaxy evolution, we push our study toward other epochs of the universe. Furthermore, we expand our search by applying the idea of the extended [O II] emission line indicating an outflow, to other optical emission lines such as [O III] $\lambda 5007$ and H α $\lambda 6563$, which are the strong emission lines in star-forming galaxies and AGNs. Although the H α emission line is not a metal emission line such as [O II] or [O III] emission, extended H α emission seen in local starbursts with strong outflow like M82 suggests that spatially extended H α emission line can also be used as an indicator for galactic-scale outflow. In fact, [Lin et al. \(2017\)](#) recently discovered a nearby galaxy with extended H α emission, which is plausibly caused by an AGN outflow. This suggests that the spatial extension of the H α emission line can be primarily used to indicate the large-scale outflow from the galaxy. With currently available narrowband and broadband imaging data from SXDS, we conduct a systematic study of large-scale outflowing galaxies selected with extended [O II], [O III], and H α emission lines and their evolution over the past 9 billion years from $z \sim 1.5$ to the present-day universe.

This paper is organized as follows. Section 2 describes the imaging data and selection methods including a new process we develop to efficiently select galaxies with extended emission lines. The results of blobs with different emission lines including spectroscopic confirmation are explained in section

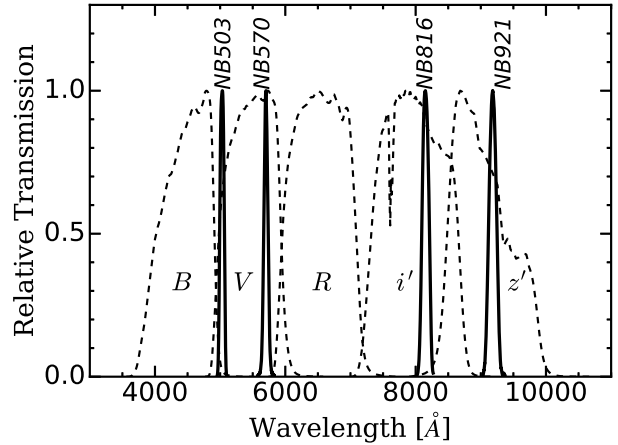


Figure 1. Peak-normalized transmission curves of Subaru/Suprime-Cam broadband $BV Ri' z'$ and narrowband $NB503$, $NB570$, $NB816$, and $NB921$ filters.

3. In section 4, we discuss in detail about the AGN contribution, stellar properties, cumulative luminosity function, and the evolution of blobs along redshifts. Finally, we summarize all results in section 5. Throughout this paper, we adopt the standard Λ CDM cosmology with $H_0 = 70 \text{ km s}^{-1} \text{ Mpc}^{-1}$, $\Omega_m = 0.3$, and $\Omega_\lambda = 0.7$. All magnitudes are given in the AB system ([Oke & Gunn 1983](#)).

2. DATA AND SAMPLE SELECTION

2.1. Imaging data

Optical data in the SXDS field are obtained with Suprimecam on the Subaru Telescope in four narrowband ($NB503$, $NB570$, $NB816$, and $NB921$; [Ouchi et al. 2008, 2009](#)) and five broadband filters (B , V , R , i' , and z' ; [Furusawa et al. 2008](#)). All data cover an area of 1.3 deg^2 in five overlapping pointings of Suprime-Cam. The combination of these filters is used to select emitters at all redshifts. Figure 1 shows transmission curves of the above filters. Near-infrared data in J , H , and K bands are obtained from data release 8 (DR8) of UKIDSS ultra deep survey (UDS; [Lawrence et al. 2007](#)) taken with WFCAM on the UK Infrared Telescope (UKIRT) and mid-infrared data in Infrared Array Camera (IRAC) channels 1 ($3.6 \mu\text{m}$) and 2 ($4.5 \mu\text{m}$) from *Spitzer* UDS survey (SpUDS; PI: J. Dunlop). The final overlapping area of Subaru and other surveys is 0.63 deg^2 ([Drake et al. 2013](#)). Table 1 summarizes crucial information of all images used in this paper including central wavelength, full width at half maximum (FWHM), and 5σ limiting magnitude.

2.2. Spectroscopic Data

We carried out spectroscopic follow-up observations for four [O III]blob candidates with Subaru/Faint Object Camera and Spectrograph (FOCAS; [Kashikawa et al. 2002](#)) on October 22–23, 2014 and December 2–4, 2015. The sky was mostly clear, expect the first-half of October 22, 2014. The on-source exposure time ranges from 7,200 to 18,000 s. The FOCAS observations were performed in MOS mode with VPH450 grating and VPH850 grating with SO58 order-cut filter. The blaze wavelengths of VPH450 and VPH850 are 4000 \AA and 8000 \AA with the spectral ranges of $3800 - 5250 \text{ \AA}$ and $5800 - 10350 \text{ \AA}$, respectively. With a slit width of $0.8''$, the resolutions are $\lambda/\Delta\lambda \simeq 1700$ and 750 for VPH450 and VPH850 gratings, respectively.

Table 1
Summary of photometric data in all narrowband and broadband filters from Subaru, CFHT, UKIRT, and *Spitzer* in SXDS field.

Telescope/Instrument	Filter	Central Wavelength (Å)	FWHM (Å)	Limiting Magnitude ^a	Reference
Subaru/Suprime-Cam	<i>NB503</i>	5029	73	24.9	Ouchi et al. (2008)
Subaru/Suprime-Cam	<i>NB570</i>	5703	68	24.5	Ouchi et al. (2008)
Subaru/Suprime-Cam	<i>NB816</i>	8150	119	25.7	Ouchi et al. (2008)
Subaru/Suprime-Cam	<i>NB921</i>	9196	132	25.4	Ouchi et al. (2009)
Subaru/Suprime-Cam	<i>B</i>	4473	1079	27.4	Furusawa et al. (2008)
Subaru/Suprime-Cam	<i>V</i>	5482	984	27.1	Furusawa et al. (2008)
Subaru/Suprime-Cam	<i>R</i>	6531	1160	26.9	Furusawa et al. (2008)
Subaru/Suprime-Cam	<i>i'</i>	7695	1543	26.7	Furusawa et al. (2008)
Subaru/Suprime-Cam	<i>z'</i>	9149	1384	26.0	Furusawa et al. (2008)
UKIRT/WFCAM	<i>J</i>	12500	1570	25.0	Lawrence et al. (2007)
UKIRT/WFCAM	<i>H</i>	16500	2910	24.3	Lawrence et al. (2007)
UKIRT/WFCAM	<i>K</i>	22000	3530	24.6	Lawrence et al. (2007)
<i>Spitzer</i> /IRAC	ch1	35500	7411	23.6	SpUDS (PI: J. Dunlop)
<i>Spitzer</i> /IRAC	ch2	44900	10072	22.9	SpUDS (PI: J. Dunlop)

^a Limiting magnitudes at 5σ in $2.0''$ diameter aperture.

2.3. Sample selection

[O II] blobs or O II_Bs at $z \sim 1.2$ in Y13 are originally selected as [O II] emitters by Drake et al. (2013) and studied in Drake et al. (2015). They isolated O II_Bs at from the normal [O II] emitters with no extended emission based on an emission-line image constructed by subtracting interpolated continuum from the narrowband image. The O II_Bs are those with isophotal area measured down to 2σ limiting surface brightness fluctuation of $28.0 \text{ mag arcsec}^{-2}$ or $1.2 \times 10^{-18} \text{ erg s}^{-1} \text{ cm}^{-2} \text{ arcsec}^{-2}$ in the emission-line image over 900 kpc^2 or approximately 30 kpc spatial extent. Visual verification was then performed to remove merging systems that can mimic the extended feature of emission.

In this paper, we follow the above processes used in Y13 and strengthen the selection process by including quantitative analysis instead of using visual verification to determine whether or not the galaxies really show the extension of the emission line beyond their stellar component. Briefly speaking, we perform a careful search of blobs according to the following processes.

- We select emitters or galaxies with strong emission lines (Section 2.3.1). Table 2 summarizes types of emission lines detected in each narrowband filter and the corresponding redshift ranges.
- Then we construct the image that contains only flux from the emission line by using broadband and narrowband images and select only emitters with a spatially extended profile (Section 2.3.2).
- Bright point spread functions (PSFs) and merging systems that can mimic the extended profile of blobs are excluded by a new quantitative method (Section 2.3.3).

2.3.1. Emitter selection

We use the sample of [O II], [O III], and H α emitters detected in four narrowband filters provided by Drake et al. (2013). Detailed procedures for selecting the emitters are described in the above paper. In short, they identified objects with potential emission lines by using the narrowband excess, i.e., *Cont-NB*, where *Cont* and *NB* are the magnitudes of objects in broadband and narrowband images, respectively. The objects showing the strong emission line are those with the narrowband excess above 3σ level relative to

Table 2

Summary of emitters in the SXDS field at each redshift bin taken from Drake et al. (2013).

Narrowband filter	Emission line	Redshift range ^a	# of emitters
<i>NB503</i>	[O II]	$0.10 < \mathbf{0.35} < 0.50$	142
<i>NB570</i>	[O III]	$0.00 < \mathbf{0.14} < 0.30$	42
<i>NB570</i>	[O II]	$0.30 < \mathbf{0.53} < 0.70$	96
<i>NB816</i>	H α	$0.00 < \mathbf{0.25} < 0.35$	152
<i>NB816</i>	[O III]	$0.35 < \mathbf{0.63} < 0.80$	985
<i>NB816</i>	[O II]	$0.80 < \mathbf{1.19} < 1.50$	1013
<i>NB921</i>	H α	$0.00 < \mathbf{0.40} < 0.50$	279
<i>NB921</i>	[O III]	$0.50 < \mathbf{0.83} < 1.10$	930
<i>NB921</i>	[O II]	$1.10 < \mathbf{1.46} < 1.90$	2204

^a Redshift ranges are photometric redshifts that are used to select emitters at each redshift bin.

Table 3

Limiting Surface Magnitudes of Emission-Line images.

Emission-line image	2σ Limiting surface magnitude/flux (AB mag arcsec ⁻² /erg s ⁻¹ cm ⁻² arcsec ⁻²)
<i>NB503-BV</i> ^a	$27.8/2.4 \times 10^{-18}$
<i>NB570-BR</i> ^b	$27.2/3.0 \times 10^{-18}$
<i>NB816-Rz</i> ^c	$28.0/1.2 \times 10^{-18}$
<i>NB921-z'</i>	$28.1/1.1 \times 10^{-18}$

^a *BV* is defined as $BV \equiv (B+V)/2$.

^b *BR* is defined as $BR \equiv (B+2R)/3$.

^c *Rz* is defined as $Rz \equiv (R+2z')/3$.

the sigma-clipped median *Cont-NB* of all objects in the images. It roughly corresponds to the observed equivalent width (EW_{obs}) of 30 \AA . The photometric redshifts are then used to categorize emitters into [O II], [O III], or H α emitters at corresponding redshifts. The numbers of emitters at redshifts ranging from $z \sim 0.1$ to $z \sim 1.5$ are listed in Table 2.

2.3.2. Blob selection

We construct the emission-line image by subtracting the continuum from the narrowband images. The continuum is determined from the broadband image at approximately the

same wavelength as the narrowband images. Before performing the image subtraction, we resemble the PSF sizes of the narrowband and broadband images by smoothing the image with a Gaussian kernel to match the other one with the largest PSF size (typically $0.8-1.0''$; Ouchi et al. 2008). The remaining flux in the subtracted narrowband images would be only from the emission line. Surface magnitude limits of the emission-line images are summarized in Table 3. The resulting images are then smoothed with the Gaussian kernel.

The isophotal areas of emitters at all redshifts are measured with SExtractor (Bertin & Arnouts 1996) down to 1.2×10^{-18} $\text{erg s}^{-1} \text{cm}^{-2} \text{arcsec}^{-2}$ to match the flux limit adopted in Y13. Figures 2 and 3 show the magnitudes and isophotal area of all emitters in the emission-line *NB816-Rz* and *NB921-z'* images, respectively.¹ The magnitudes in the *NB816-Rz* and *NB921-z'* images indicates fluxes of the continuum-subtracted emission line. It is important to note that the object with higher flux (lower magnitude) in the *NB816-Rz* or *NB921-z'* image is not necessarily more luminous in the broadband image, which shows the stellar continuum. We separately plot $\text{H}\alpha$, $[\text{O II}]$, and $[\text{O III}]$ emitters, in different panels for clarity. The uncertainty of the isophotal area is determined by Monte Carlo simulations as in Y13. We cut out postage-stamp images of the blobs and place them randomly on ~ 1000 sky regions of the emission-line image and re-measure their isophotal areas. The errors shown in the figures are 1σ of the isophotal area distributions.

According to the figures, the isophotal area increases with the brightness of the emitters, but most of the emitters have small isophotal area in the emission-line images. A blob candidate is an emitter whose isophotal area in the emission-line image is larger than 900 kpc^2 or 30-kpc spatial extent. We also select the blob candidates with extremely large extension with the higher isophotal area criterion of 1500 kpc^2 . Some emitters with isophotal area larger 900 kpc^2 are excluded during the methods explained below.

2.3.3. Quantitative approaches to securely select blobs

Bright objects and merging systems can mimic the appearance of extended emission in the emission-line images. If the object is bright enough, it can be falsely classified as a blob candidate. On the other hand, small emitters located very close to each other can be seen as one extended object in the smoothed emission-line images. It is therefore necessary to carefully examine every single blob candidate. In Y13, they visually verified the continuum components of each blob candidate. However, visual verification is time consuming and is potentially affected by personal bias. In this paper, we develop the following quantitative methods to identify the blobs with genuinely extended emission.

- *Discrimination of bright PSF-like emitters*

Isophotal area of an object normally depends on its brightness; the brighter object tends to show larger isophotal area as seen in Figures 2 and 3. Bright compact emitters may have large isophotal area. In order to distinguish the bright PSF-like emitters with large isophotal area from the blobs, we create a mock sample of PSFs with uniform distribution of emission-line magnitudes ranging from 20 to 25 mag and insert them

¹ Note that we do not show the isophotal area plots of *NB503-V* and *NB570-V*, because no emitter in these two narrowband filters shows the isophotal area larger than 900 kpc^2 .

randomly into the original emission-line images. We reselect the artificial objects and examine their isophotal area and magnitudes using the identical criteria as used for emitters. The resulting 1σ distributions are shown as the shaded area in the figures. We exclude all emitters falling into the shaded regions from final samples of blobs.

Another issue in selecting blob candidates is nearby objects. If there is an object located close to the emitters, they could appear as one extended object in the emission-line images and can be falsely classified as a blob. We examine the effect of multiple objects located close to each other by simulating two closeby PSFs either the same magnitudes separated at various distances or with different magnitudes separated at a fixed distance. Figure 4 shows 1σ standard deviation of the isophotal area of the simulated PSFs. With the full width at half maximum (FWHM) of $\sim 0.8''$, the isophotal area of the artificial PSFs becomes largest at $2.0''$ separation and goes down to be approximately identical to the isophotal area of one PSF at smaller or larger separations. At a distance larger than $2.0''$ two PSFs are detected as separate sources. Their isophotal areas are thus similar to those of one PSF. The results are common in all emission-line images regardless of the observed wavelengths. As a $2.0''$ separation of PSFs gives the largest isophotal area, we further simulate two PSFs with varying magnitude at the fixed $2.0''$ separation. We found that the isophotal area tends to decrease and become comparable to that of one PSF when we increase the magnitude difference between two simulated PSFs. We apply these results to blob candidates with nearby continuum components.

After the emitters pass the isophotal criterion, we first check the number of continuum components each blob candidate has. If it has only one continuum counterpart, we examine if its isophotal area exceeds the 1σ isophotal-area distribution of the PSF (grey shaded region in the figures). If the blob candidate has two continuum components, we further determine the separation between those components and check if the isophotal area of the candidate is larger than the results of PSF simulations (Figure 4). The candidates that do not satisfy these PSF criteria are shown as the black dots above 900 kpc^2 in the figure. Finally, if there are more than two components, we will use the next method to classify whether the emission is spatially extended or not. The blobs with multiple components that pass all criteria are indicated with colored symbols enclosed by thick black squares and circles in Figures 2 and 3, respectively.

- *Final selection of blobs using equivalent width map*

To further secure the blob sample, we develop a new approach to prove the emission-line extension beyond the stellar component. We construct an equivalent width (EW) map for the individual blob candidate obtained after passing the above criteria. The observed equivalent width of an emission line is generally defined as $\text{EW}_{\text{obs}} = F_{\text{line}}/f_{\lambda,\text{cont}}$, where F_{line} and $f_{\lambda,\text{cont}}$ are flux of the emission line and flux density of the continuum at the same wavelength, respectively. We use the emission-line images listed in Table 3 to estimate fluxes

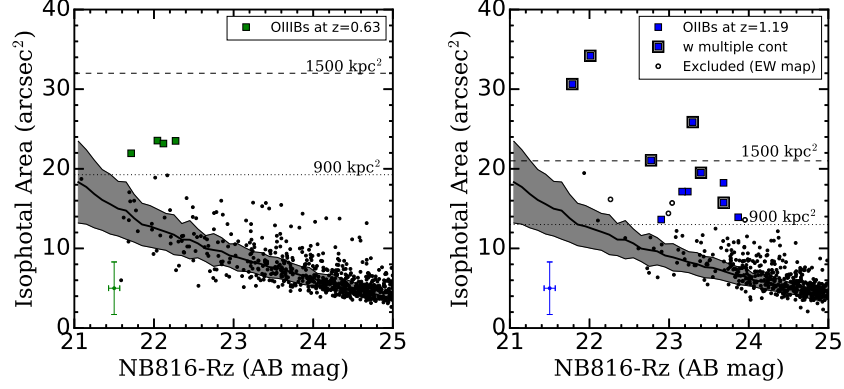


Figure 2. Isophotal area-magnitude plot of the $NB816-Rz$ images for $O\ III$ s at $z \sim 0.63$ (left) and $O\ II$ s at $z \sim 1.18$ (right). Green and blue squares represent the $O\ III$ s and $O\ II$ s at respective redshifts. Dotted symbols are all emitters at corresponding redshifts. Those above the criteria of $900\ kpc^2$ are the emitters the large isophotal area of which is caused by multiple continuum components. They are excluded from the final blob sample by the PSF simulation (Section 2.3.3). Open circles are the emitters that are ruled out from the final blob sample according to the EW-map criterion. Dotted and dashed lines show isophotal criteria used to select the blobs at $900\ kpc^2$ and $1500\ kpc^2$, respectively. Blobs with multiple continuum components are enclosed by black square symbols. Error bars on the bottom left corner of the figures indicate typical errors of magnitudes and isophotal area. The grey regions show 1σ distribution of the simulated PSFs.

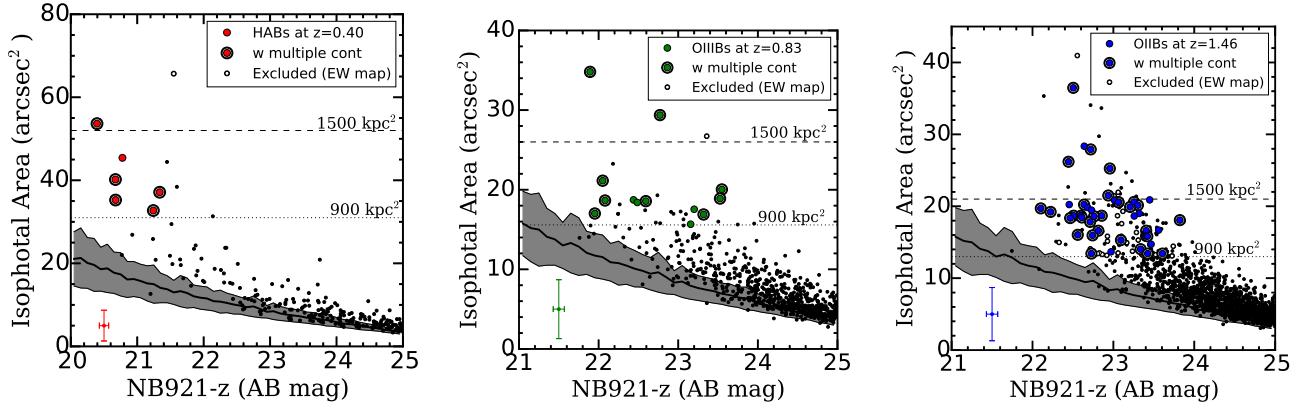


Figure 3. Isophotal area-magnitude plot of the $NB921-z'$ images for $H\alpha$ emitters at $z \sim 0.40$ (left), $[O\ III]$ emitters at $z \sim 0.83$ (middle), and $[O\ II]$ emitters at $z \sim 1.46$ (right). Red, green, and blue circles represent the corresponding blobs at respective redshifts. Other symbols are the same as described in Figure 2.

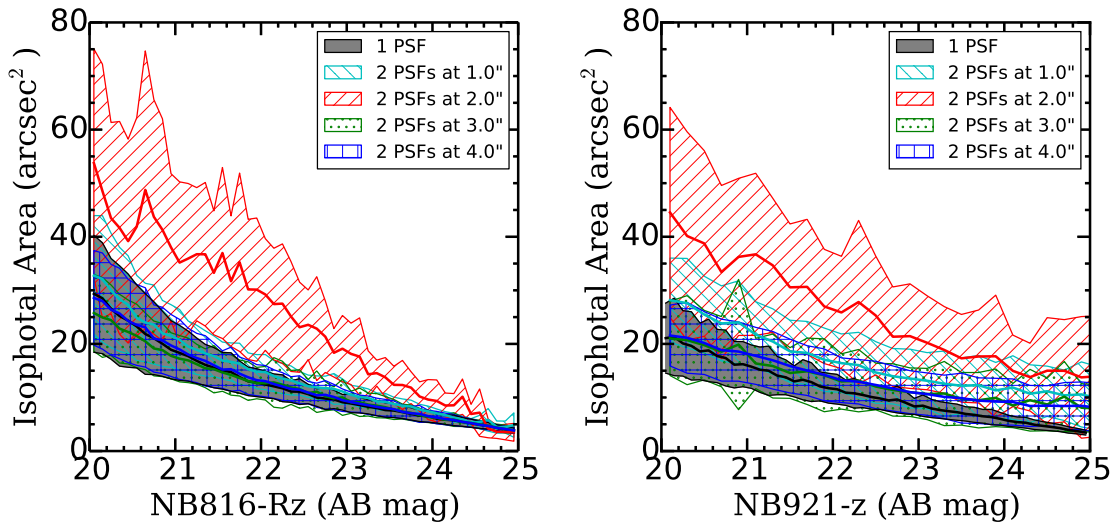


Figure 4. Isophotal area-magnitude plot of two simulated PSFs put close to each other in $NB816-Rz$ (left) and $NB921-z'$ (right) images. The two PSFs are simulated with identical magnitude separated at $1.0''$, $2.0''$, $3.0''$, and $4.0''$ distances from each other. The average isophotal areas are shown in thick lines, while the shaded regions represent 1σ distributions. Simulation of one PSF is also shown with grey shaded region.

of the emission lines and the corresponding broadband images to construct the EW map. The basic idea of using the EW map is that the EW of the extended region is enhanced due to relatively low flux density of the stellar continuum.

Kornei et al. (2012) studied star-forming galaxies at $0.7 < z < 1.3$ in the Extended Groth Strip (EGS) field and reported the average rest-frame [O II] EW of 45 Å. More than 90% of their sample shows an [O II] EW less than 100 Å (their Figure 1). The star-forming region, where the stellar component is located, is unlikely to produce the [O II] emission with the rest-frame EW as high as 100 Å. Therefore, we adopt the rest-frame [O II] EW criterion of > 100 Å to define the isophotal area as real extended emission. For the [O III] emission line, we apply the ratio between [O II] and [O III] emission lines of [O III]/[O II] = 0.3, which is the typical line ratio of star-forming galaxies at $z \sim 1.2$ (Harikane et al. 2014) and adopt [O III] EW larger than 30 Å as a criterion. The $H\alpha$ EW criterion is derived from the [O II] EW by using the relation between SFR and the emission lines by Kennicutt (1998). It is noteworthy that the EW value above criteria in the EW map does not directly correspond to the EW of the blob. It simply indicates that the pixel with that EW is either the extended emission with no/faint stellar component or just noise of the image.

In case of a compact, PSF-like source, the number of pixels with an EW higher than the above criteria is ideally supposed to be zero, because of no extended emission line. In fact, it is not exactly zero due to the noise around the object. We investigate the distribution of the PSFs containing the pixels with high EWs in the emission-line image in order to determine the minimum number of pixels whose EW is enhanced by the noise in one PSF. We create EW maps of the isolated PSFs with the narrowband magnitudes of 20–24 mag and measure the numbers of pixels with EW higher than the criterion for each emission line. Normalized histograms of the PSFs with the numbers of pixels having EW above criteria are shown in Figure 5. As a point source with no extended feature, the simulated PSFs should not have any pixel with high EW. The number of pixels that have the EW larger than the criteria in the PSFs can be considered as the possible noise we could obtain when counting the pixels with high EW. Almost more than 60% of the simulated PSFs in the *NB816-Rz* image have less than 40 pixels with the EW higher than the criteria. However, a fraction of PSFs contains larger numbers of pixels with the EW above the criteria. For the *NB921-z'* image, the simulated PSFs have more pixels with the EW above the criteria, but a majority of them still show small numbers of pixels with high EW. The blob with a genuinely extended emission line should consist of pixels with large EW more than at least 1σ distribution of the PSF noise (thick vertical dashed lines in Figure 5).

Figure 6 shows comparison between O IIB1 at $z \sim 1.2$ by Y13 and the normal [O II] emitter with no extension of the emission at the same redshift that can be falsely identified as a blob if we only use the isophotal area criterion. The [O II] emitter at $z \sim 1.2$ in the bottom

panel shows the isophotal area of 16 arcsec² or physically 1108 kpc² in the *NB816-Rz* image. It is larger than the isophotal area criterion we set for O IIBs at $z \sim 1.2$ (> 13 arcsec² or 900 kpc²). This [O II] emitter would be selected as an [O II] blob according to its isophotal area. However, as seen in Figure 6, the large isophotal area of the emitter is simply caused by multiple nearby objects. When we smooth the emission-line images with the Gaussian kernel to reduce the fussy noise, the nearby objects are blended together and detected as one huge source. We are able to get rid of these objects by using the EW map. We set the EW per pixel to be larger than 100 Å for [O II] emission and the number of pixels with the EW higher than this criterion needs to exceed 104 pixels (Figure 5). As seen in the EW map in the right panel of Figure 6, the pixels with the rest-frame [O II] EW higher than 100 Å are only the trivial noise at the edge of isophotal area. As a result, this object is not satisfied the EW-map criterion. In contrast, O IIB1 in the top panel of the figure shows significantly large number of pixels with rest-frame EW higher than 100 Å. With this method, we are able to accurately identify the blobs with spatially extended emission lines. The final sample of blobs is shown with colored symbols in Figures 2 and 3. The emitters that are excluded from the final blob sample because of the EW-map criterion are indicated with open black circles.

3. RESULTS

Although we search for the possible blobs with extended [O II], [O III], and $H\alpha$ emission lines from $z \sim 0.14$ to $z \sim 1.46$, $H\alpha$ blobs or HABs at $z = 0.40$ are the blob samples at the lowest redshift we could acquire. The final samples of O IIBs, O IIBs, and HABs at $z \sim 0.4$ –1.5 are summarized in Table 4. As seen in the table, it is obvious that the number of blobs decreases significantly if we consider only the larger isophotal area. Coordinates, magnitudes, luminosity, and isophotal area of the emission lines of all blob samples are listed in Appendix. It is noteworthy that the IDs of blobs are assigned to describe types of blobs (i.e., O IIB, O IIB, or HAB), the redshifts, number of stellar components (single or multiple), and the number starting from 1 for the largest blob. For example, HAB040m-1 means that this galaxy is the largest HAB with multiple stellar components at $z = 0.40$.

3.1. HABs at $z = 0.40$

At $z = 0.40$, there are in total 6 HABs selected with isophotal area above 900 kpc², but only one object, which we call HAB040m-1, shows the $H\alpha$ emission extended over 1500 kpc². Specifically, the isophotal area of HAB040m-1 is 1549 kpc², roughly corresponding to 40 kpc across (Figure 7). This object is spectroscopically confirmed to be at $z = 0.407$ (Simpson et al. 2012). The extended $H\alpha$ flux of this blob is 1.18×10^{-15} erg s⁻¹ cm⁻². The $H\alpha$ luminosity is 6.94×10^{41} erg s⁻¹. HAB040m-1 is also identified as a radio source with 1.4-GHz flux density of ~ 120 μ Jy (Simpson C. in private communication). Hence HAB040m-1 is likely to be powered by an AGN. Unfortunately, we do not have the X-ray data covering this object. As seen in the middle panel of Figure 7, HAB040m-1 seems to show collimated $H\alpha$ emission in the direction perpendicular to its continuum component. This structure is similar to that of M82, which is the prototypical

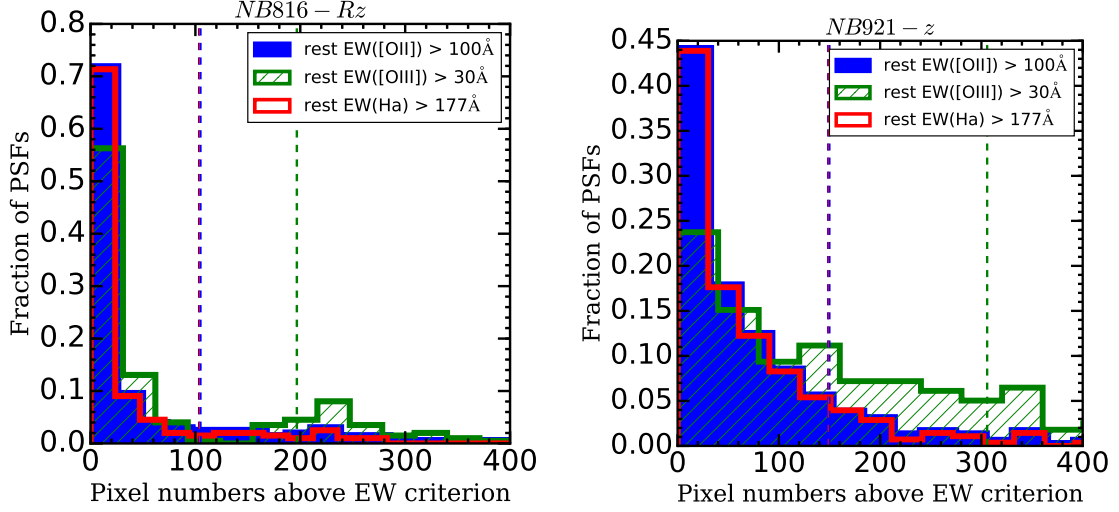


Figure 5. Normalized histograms of the simulated PSFs with the pixels that have the EW above the criteria for [O II] (blue), [O III] (green), and H α (red) emission lines in the *NB816-Rz* (left) and *NB921-z'* images (right). The number of pixels in one PSF is shown on the x axis. Dashed lines indicate 1σ standard deviations that are used as the EW criteria. Note that the blue and red histograms are almost identical to each other and are difficult to distinguish by eyes.

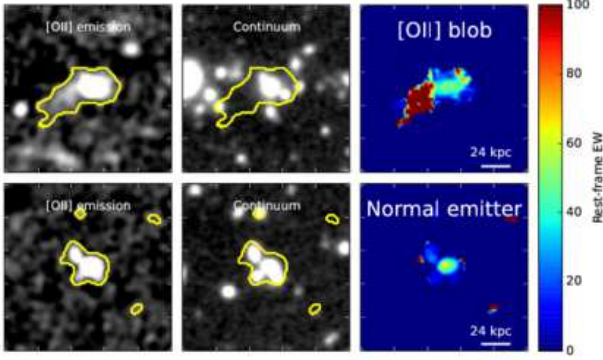


Figure 6. O II B1 at $z \sim 1.2$ and the normal [O II] emitter at the same redshift with multiple nearby objects that make the emitter appear as an extended source in the emission-line image. *Left and middle panels:* Emission-line (*NB816-Rz*) and continuum (*Rz*) images. Yellow contours represent the isophotal area of the objects measured in the smoothed emission-line images. *Right panel:* The EW maps of the objects. The color bar indicates the rest-frame EW of the emission line in each pixel. The white bar at the bottom right of the figure shows a physical scale of 24 kpc by assuming the redshift at $z \sim 1.2$.

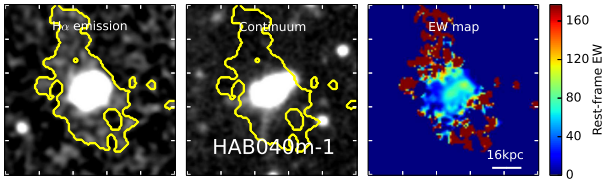


Figure 7. From left to right, the emission-line (*NB921-z'*), continuum (z), and EW map images of an HAB at $z = 0.40$ with H α isophotal area larger than 1500 kpc^2 . The ID of the HAB is indicated in the middle panel. Yellow contours on the left and middle panels show the isophotal area of the blob above $1.2 \times 10^{-18} \text{ erg s}^{-1} \text{ cm}^{-2} \text{ arcsec}^{-2}$ measured in the smoothed emission-line image. Note that we do not take the small regions of the contours shown in the middle and bottom panels into account when classifying the blobs. The color bar on the right panel indicates the rest-frame equivalent width of H α emission. The white bar on the right panel represents the physical scale of $\sim 16 \text{ kpc}$. In all panels, North is up and East is to the left.

starburst galaxy with large-scale outflow in the local universe (see Figure 2 in [Walter et al. 2002](#)). A follow-up study is necessary to examine the outflow properties and the energy

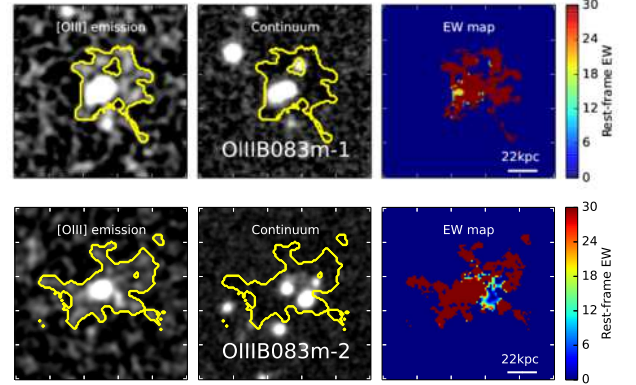


Figure 8. Same as Figure 7 but for O III B1s at $z = 0.83$ with isophotal area of [O III] emission larger than 1500 kpc^2 . The white bar on the right panel represents the physical scale of $\sim 22 \text{ kpc}$.

source.

3.2. O III B1s at $z = 0.63$ and $z = 0.83$

Four and thirteen [O III] blobs or O III B1s with the isophotal area of [O III] emission over 900 kpc^2 are obtained at $z = 0.63$ and $z = 0.83$, respectively. Among them, only two O III B1s at $z = 0.83$ show the extended [O III] emission line larger than 1500 kpc^2 . The top panel of Figure 8 shows the largest O III B1 at $z = 0.83$ (O III B083m-1), whose [O III] emission line covers approximately 2010 kpc^2 . In the bottom panel, the second largest O III B1, O III B083m-2, shows the extended emission line of $\sim 1700 \text{ kpc}^2$. As seen in the figure, there are two objects located close to the O III B1. Both objects are not at $z = 0.83$ according to their photometric redshifts. The EW map in the bottom right panel of Figure 8 in which the red part indicates the components with high [O III] EW suggests that these nearby objects are not responsible for the extended [O III] emission. So the extension is likely to come from the O III B1.

3.3. O II B1s at $z = 1.19$ and $z = 1.46$

At higher redshifts ($z > 1$), blobs are selected with the extended [O II] emission line. Y13 firstly discovered 12 O II B1s

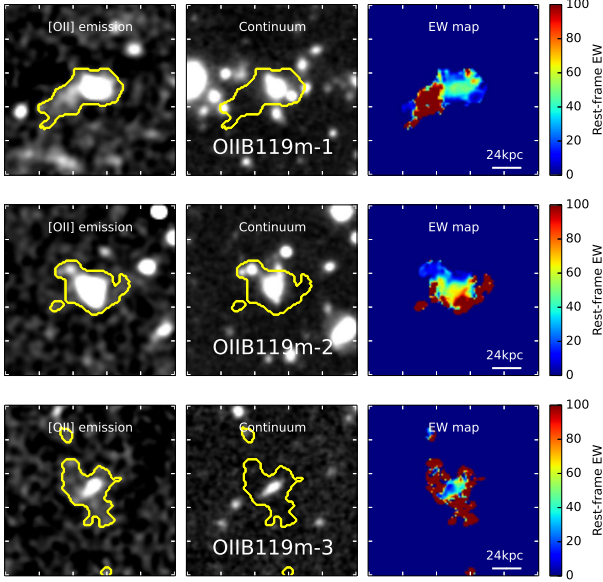


Figure 9. Same as Figure 7 but for O II B119m-1, O II B119m-2, and O II B119m-3 at $z = 1.19$ with isophotal area of [O II] emission larger than 1500 kpc^2 . The white bar on the right panel represents the physical scale of $\sim 24 \text{ kpc}$.

at $z = 1.19$. Now we select 11 O II B119m-1, O II B119m-2, and O II B119m-3 at this redshifts. The difference in the O II B numbers between Y13 and our paper is mainly due to additional quantitative criteria of bright PSFs and EW maps that we apply to ensure the extended feature of [O II] emission. We now have a more secure sample of [O II] blobs with extended emission lines. Figure 9 shows three O II B119m-1, O II B119m-2, and O II B119m-3 at $z = 1.19$ with isophotal area of the [O II] emission line larger than 1500 kpc^2 . The O II B with the largest extension of the [O II] emission line in the top panel of Figure 9 is O II B119m-1, which is spectroscopically identified to be an outflowing obscured AGN at $z = 1.19$ by Y13 (O II B1 in Y13). The extended [O II] emission line is clearly seen in the EW map. The middle panel shows the second largest O II B at the same redshift, O II B119m-2. It is seen in the figure that the area with an EW larger than the criterion is not due to the nearby object. This object is thus identified as the O II B. The third largest O II B, O II B119m-3, is shown in the bottom panel of Figure 9. The stellar component of this O II B appears as an edge-on galaxy, while the [O II] emission line extends in the direction perpendicular to the shape of the continuum, similar to the extended H α emission line of HAB040m-1 in section 3.1 and M82.

The highest redshift that we search for the blobs in this paper is $z = 1.46$. Applying the same surface flux density limit at each redshift studied, we select 43 objects with the isophotal area of the [O II] emission line larger than 900 kpc^2 as O II B146m-1, O II B146m-2, O II B146m-3, O II B146m-4, O II B146m-5, and O II B146m-6 at $z = 1.46$, six of which show even more extended emission over 1500 kpc^2 (Figure 10). The figure is arranged in order of the blob size. The O II B with the largest isophotal area is in the top panel of the figure, while the smallest one is shown in the bottom panel. The largest O II B at $z = 1.46$, O II B146m-1, is shown in the top panel of Figure 10. The extended [O II] emission line of this O II B is clearly seen. The isophotal contour of the second largest O II B (O II B146s-2) shown in the second panel from the top of the figure is in the strange shape because it is very close to the other object, which is also identified as an [O II] emitter at the same redshift. This is an interesting case in the sense that the O II B

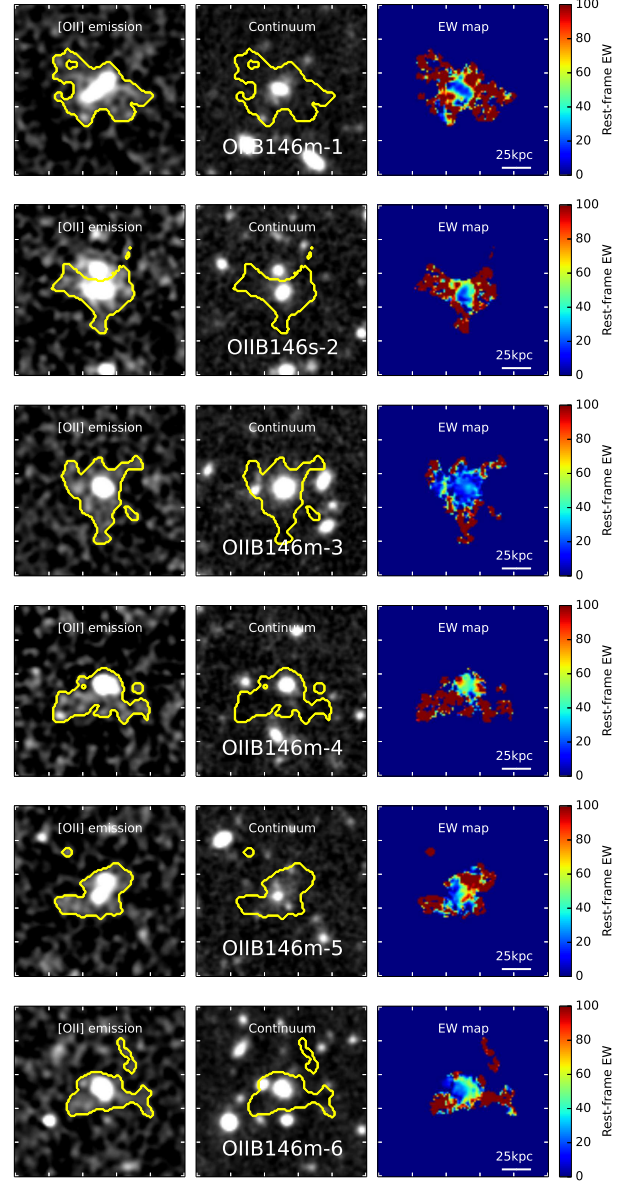


Figure 10. Same as Figure 7 but for O II B146m-1, O II B146m-2, O II B146m-3, O II B146m-4, O II B146m-5, and O II B146m-6 at $z = 1.46$ with isophotal area of [O II] emission larger than 1500 kpc^2 . The white bar on the right panel represents the physical scale of $\sim 25 \text{ kpc}$.

may consist of two galaxies that are about to merge or in the middle of merging process. We can also consider both emitters as one O II B with multiple stellar components. It will not affect the total number of O II B146m-1, O II B146m-2, O II B146m-3, O II B146m-4, O II B146m-5, and O II B146m-6 at $z = 1.46$. The third O II B O II B146m-3 is similar to the first one in the way that it has only one stellar component with significant extended [O II] emission. However, the only difference between these two blobs is that O II B146m-3 seems to show extended emission in almost all directions, while the [O II] emission in the O II B146m-1 looks like bimodal outflow. The remaining 3 O II B146m-4, O II B146m-5, and O II B146m-6 at $z = 1.46$ seem to show an asymmetric extension of the [O II] emission line. The shapes of the emission of all O II B146m-1, O II B146m-2, O II B146m-3, O II B146m-4, O II B146m-5, and O II B146m-6 may suggest that the extended emission can occur in different directions depending on the galaxies.

3.4. Spectroscopic Confirmation

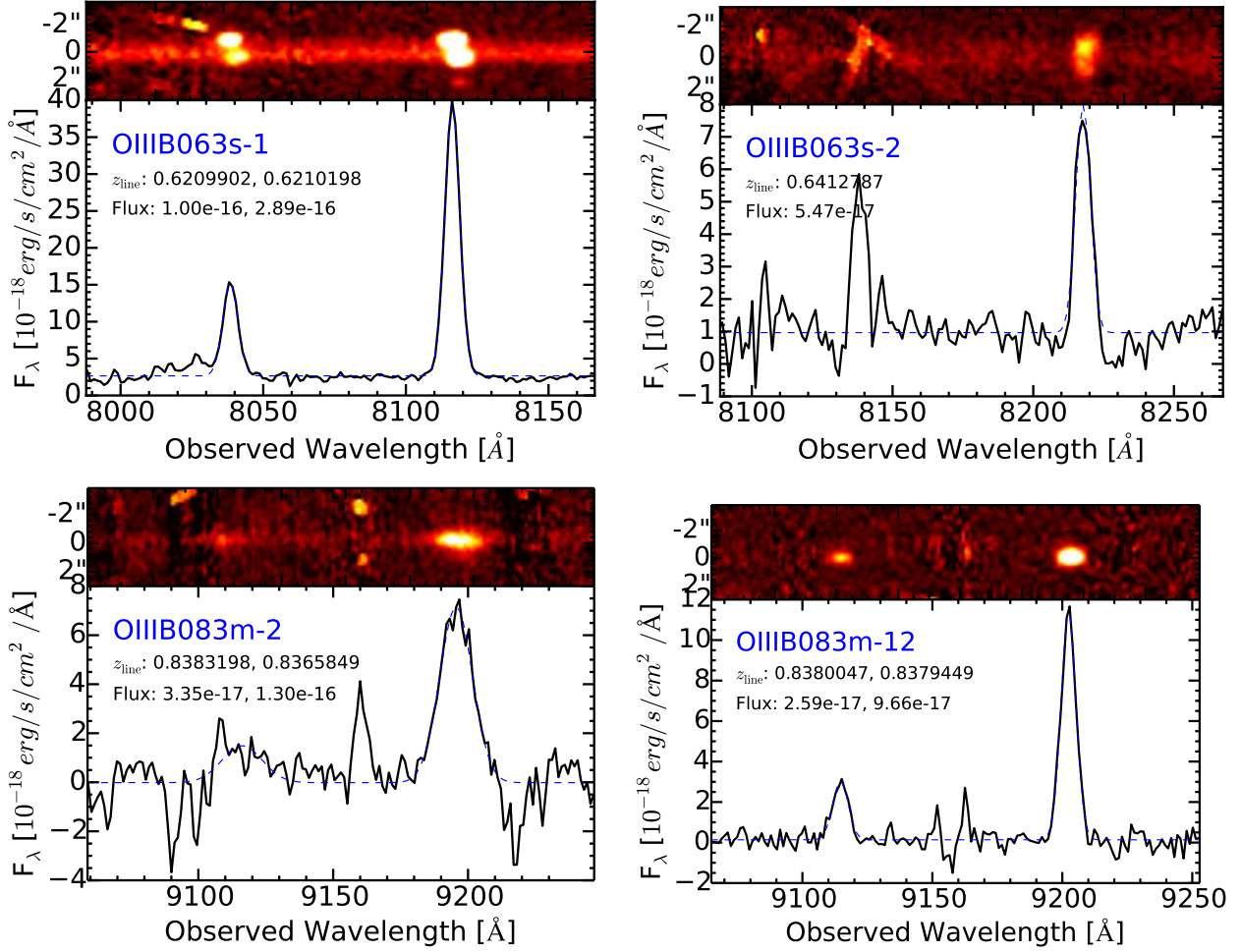


Figure 11. Subaru/FOCAS Spectra of O III B at $z = 0.63$ (top panels) and at $z = 0.83$ (bottom panels) in the observed frame. Each panel shows the O III B spectrum covering [O III] $\lambda\lambda$ 4959, 5007 emission lines in black solid line and the best-fit Gaussian profile in blue dashed line. The corresponding two-dimensional spectrum is also shown at the top of the panel. Redshifts and observed fluxes of the emission lines are indicated.

Table 4

Summary of final sample of blobs in the SXDS field.

Redshift	Emission line	Number of blobs ^a	
		> 900kpc ²	> 1500kpc ²
0.40	H α λ 6563	6 (2/33%)	1 (1/100%)
0.63	[O III] λ 5007	4 (0)	0 (0)
0.83	[O III] λ 5007	13 (0)	2 (0)
1.19	[O II] λ 3727	11 (2/18%)	3 (2/67%)
1.46	[O II] λ 3727	43 (4/9%)	6 (2/33%)

^a Parentheses show the number of blobs with X-ray (0.5–10 keV) or radio (1.4GHz) counterpart, which are considered to host AGNs, and the percentage of possible AGN fraction.

We perform the spectroscopic follow-up observations for 4 O III B at $z = 0.63$ and $z = 0.83$ (Section 2.2). Due to the limited observing time, we prioritize our follow-up observations to the blobs with the largest extension at each epoch and simultaneously maximize the number of blobs in one MOS mask. As a result, we obtain the spectra of two largest O III B at $z = 0.63$ (O III B063s-1 and O III B063s-2), the second largest O III B (O III B083m-2), and one small O III B (O III B083m-12) at $z = 0.83$. Their [O III] spectra are shown in Figure 11.

We carefully investigate the possibilities of Ly α , [O II], and H α emitters at other redshifts. At $z = 0.63$, the O III B should exhibit an emission line at ~ 8100 \AA falling into the NB816 narrowband filter. If it is [O III] λ 5007 emission, we should observe the doublet with an [O III] λ 4959 emission at the shorter wavelength. For the largest blob at $z = 0.63$ (O III B063s-1), we detect another emission line at ~ 8045 \AA , which perfectly corresponds to [O III] λ 4959 emission. Furthermore, we also detect the [O II] emission line at ~ 6040 \AA . Therefore, O III B063s-1 is spectroscopically confirmed to be at $z = 0.621$. For O III B063s-2, we detect an emission line at ~ 8200 \AA . It is confirmed to be [O III] λ 5007 at $z = 0.641$, because we detect [O II] λ 3727 line at ~ 6120 \AA .² Similarly, we detect [O III] λ 4959, 5007 doublet at ~ 9120 \AA and ~ 9200 \AA and the [O II] λ 3727 emission at ~ 6850 \AA for two O III B at $z = 0.83$ (O III B083m-2 and O III B083m-12) shown in the bottom panels of Figure 11. They are both at $z = 0.838$.

Two-dimensional spectra are also displayed at the top of each panel in Figure 11. The [O III] emission lines of the O III B are significantly more extended than the stellar continuum, especially O III B063s-1. Two components of emis-

² Note that the resolution of the spectrum is insufficient to distinguish the [O II] doublet.

sion line are obviously seen. Both components are roughly at the same redshift of $z = 0.61$, suggesting that O III B063s-1 is probably a merging system, even though only one stellar component has been detected in the broadband continuum image. Further analysis and discussion on the spatial profiles of emission lines and the outflow signature will be in the upcoming paper (Yuma et al. in prep.).

4. DISCUSSION

4.1. Primary Check for AGN Fraction

An AGN is one of the most energetic objects in the universe. It is highly plausible that the O IIBs, O IIIBs, and HABs at $z = 0.4-1.5$ we obtain in the previous section are partially or entirely powered by the AGN. In fact, Y13 found that one of their 12 O IIBs at $z \sim 1.2$, O IIB1, is a radio-quiet obscured type-2 AGN. In this section, we primarily investigate whether or not the spatially extended emission line of the blobs is due to an AGN by cross-checking our blobs with X-ray and radio source catalogs.

The SXDS X-ray data in the 0.2–10 keV band were taken with the European Photon Imaging Camera (EPIC; [Strüder et al. 2001](#); [Turner et al. 2001](#)) on board *XMM-Newton* ([Jansen et al. 2001](#)). [Ueda et al. \(2008\)](#) created the X-ray source catalog from these data down to sensitivity limits of 6×10^{-16} , 8×10^{-16} , 3×10^{-15} , and 5×10^{-15} erg s $^{-1}$ cm $^{-2}$ in the 0.5–2, 0.5–4.5, 2–10, and 4.5–10 keV bands, respectively. These flux limits roughly correspond to the X-ray luminosities of $10^{41} - 10^{42}$ erg s $^{-1}$ at $z = 0.40$ and 10^{43} erg s $^{-1}$ at $z = 1.46$, which are one order of magnitude brighter than the faint end of X-ray luminosity functions (XLFs) of AGNs at similar redshifts (e.g., [Aird et al. 2015](#); [Ranalli et al. 2016](#); [Fotopoulou et al. 2016](#)). We identify the X-ray sources that are within 3'' radius of the blobs at $z = 0.4-1.5$ as the X-ray counterparts. The reason why we use 3'' radius is that it is a typical half width at half maximum of the PSFs in *XMM-Newton* images ([Strüder et al. 2001](#)). However, we sometimes use larger radius to identify the X-ray counterpart, if the position uncertainty of the X-ray source is higher than 3''.

The VLA/1.4 GHz radio catalog is provided by [Simpson et al. \(2006\)](#). The flux density limit is 100 μ Jy. Because the typical beam size in the radio image is 5×4 arcsec 2 , we cross-match the radio sources with 2.5'' radius.

The numbers of blobs that have X-ray and/or radio counterparts are listed in the parentheses in Table 4. We consider the blob as an AGN host if it has either an X-ray or radio counterpart. According to Table 4, a fraction of blobs which possibly host an AGN increases with the isophotal area of the extended emission line. This trend is seen in all types of emission lines, probably because an AGN is able to provide energy high enough to drive the gas out of the galaxy. AGNs typically show [O III]/[O II] ratios larger than 1.0, which is higher than the star-forming galaxies with no AGN activity ([Lamareille 2010](#)). Thus O IIIBs are expected to host AGNs in a larger fraction than those of other types of blobs. However, no X-ray or radio counterpart is found for O IIIBs at $z = 0.63-0.83$. [O III] emission is a high excitation emission line. One possibility is that the O IIIBs are too faint to be detected in the X-ray catalog we use. As mentioned above that the luminosity limits of the catalog are significantly brighter than the faint end of the XLFs, many AGNs at the similar redshifts show X-ray luminosity lower than the limits of our catalog. Another possibility might be the photoionized light echo from the AGN phase that still travels across the galaxy after the

black hole at the center stops accreting (e.g., [Schawinski et al. 2015](#)). In this case, the extended [O III] emission is a leftover from the past AGN activity, while the AGN already stops emitting the X-ray after the AGN phase. Besides an AGN, there are another possible factors responsible for high [O III]/[O II] ratio such as a low metallicity ([Overzier et al. 2009](#)), a high ionization parameter ([Kewley et al. 2013](#)), and the density bounded H II region ([Nakajima & Ouchi 2014](#)). It is noteworthy that we cannot completely identify all AGNs with only X-ray and radio imaging data. There are probably O IIBs, O IIIBs, or HABs hosting X-ray-faint, radio-quiet, and/or heavily obscured AGNs. Therefore, the AGN percentages listed in Table 4 can be considered as a lower limit of AGN fraction on blobs.

4.2. Stellar properties

Photometry of the selected blobs is obtained in 10 bands: *BVRizJHK*, IRAC ch1 (3.6 μ m) and ch2 (4.5 μ m) bands. For the photometry in optical and near-infrared wavelengths, we perform source detection by using the *K*-band image and measured the magnitudes at 2.0'' diameter aperture at the identical positions in all other images using the dual mode of SExtractor. The total magnitudes of the objects are obtained by scaling the aperture magnitude in *K* band to match MAG_AUTO from SExtractor. The photometry in mid-infrared wavelengths (i.e., IRAC 3.6 and 4.5 μ m) is determined from the aperture magnitude at 2.4'' diameter, which provides the highest signal-to-noise ratio. The total magnitude in IRAC is obtained by applying the aperture correction factor that is determined by generating artificial objects with given magnitudes on the IRAC images and measuring their aperture magnitudes at 2.4'' diameter. To avoid the effect of strong nebular emission on the SED fitting, we exclude the photometry in i' or z' band from the fit depending on the narrowband filters used to originally select the blobs (i.e., *NB816* or *NB921*, respectively). It is noteworthy that excluding the photometry in either i' or z' band does not affect the resulting stellar masses of blobs. We make a comparison of the stellar masses with those derived by using the photometry in all broadband filters and those using the photometry from which the contribution of strong emission lines (i.e., [O II], [O III], and H α) is excluded. The resulting stellar masses are comparable within 0.3 dex and 0.2 dex, respectively, with no systematic offset.

The stellar populations of blobs are examined by fitting the observed photometry (spectral energy distributions; SEDs) with the stellar population synthesis models constructed with [Bruzual & Charlot \(2003\)](#) code. We assume the [Salpeter \(1955\)](#) initial mass function with standard lower and upper mass cutoffs of 0.1 M_{\odot} and 100 M_{\odot} , respectively, dust attenuation by [Calzetti et al. \(2000\)](#), and solar metallicity. We adopt the spectroscopic redshifts when available, otherwise we fix the redshifts by assuming that the emission line of each type of blobs falls into the center of the narrowband filter. We create the model SEDs with constant star formation history and perform the fitting by using SEDfit code by [Sawicki \(2012\)](#).

Figure 12 shows normalized histograms of the resulting stellar masses of the blobs from $z = 0.40$ to $z = 1.46$. For comparison purpose, we also plot the stellar-mass histograms of all emitters (including blob samples) in the figure. In order to make an unbiased comparison, we compare the SED fitting results of the blobs with those of the emitters that have the same emission-line fluxes (i.e., the same *NB816-NB921-z'* magnitude). In other words, the comparison is

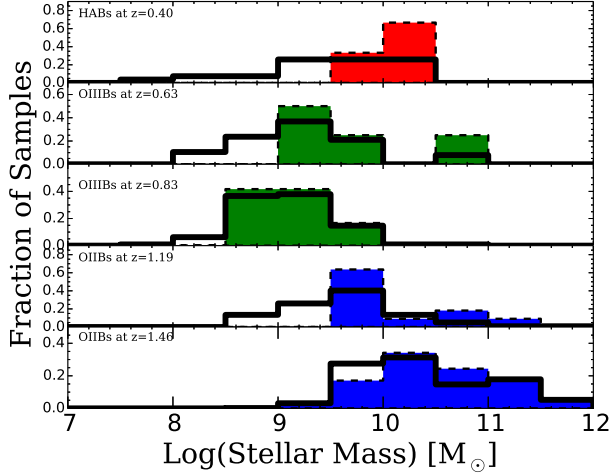


Figure 12. Normalized histograms of stellar masses for blobs and emitters at $z = 0.40 - 1.46$. Blobs are shown with colored histograms, whereas open ones are for the emitters at the corresponding redshifts. The histograms are normalized in the way that they show the fraction of blobs/emitters in each mass bin. Types and redshifts of blobs/emitters are indicated in each panel.

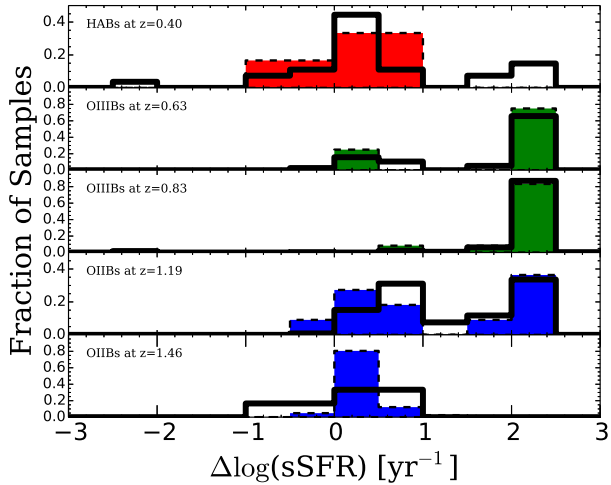


Figure 13. Normalized histograms of $\Delta \log(\text{sSFR})$ compared to the main sequence at $z \sim 1$ by Elbaz et al. (2007) for blobs and emitters at $z = 0.40 - 1.46$. The meanings of symbols are identical to those in Figure 12.

performed for the $\text{H}\alpha$, $[\text{O III}]$, $[\text{O II}]$ blobs/emitters with the corresponding line fluxes of $3 - 12 \times 10^{-16}$, $0.5 - 4 \times 10^{-16}$, and $0.4 - 5 \times 10^{-16} \text{ erg s}^{-1} \text{ cm}^{-2}$, respectively. The histograms are normalized to show the fraction of blobs or emitters in each mass bin. It is seen at all redshifts that the blobs have obviously larger stellar masses than the emitters at the same redshift. At $z = 0.40$, $\text{H}\alpha$ emitters have the stellar masses ranging from $\sim 5 \times 10^7 M_\odot$ to $\sim 5 \times 10^{10} M_\odot$, while HABs are located only at the massive end of the distribution. We perform the Kolmogorov-Smirnov (KS) test to examine if the histograms of HABs and $\text{H}\alpha$ emitters are drawn from the same distribution. We can reject the null hypothesis that they are from the same distribution at the 90% confidence level. Similarly, we can reject the null hypothesis for being drawn from the same distributions at the 99% confidence level for OIIbBs at $z = 1.19$ and at the 90% confidence level for OIIbBs at $z = 1.46$. On the other hand, we cannot reject the null hypothesis that OIIIbBs at $z = 0.63$ and at $z = 0.83$ are drawn from the same stellar mass distributions as the emitters

at corresponding redshifts. In addition to the KS test, we perform the Anderson-Darling (AD) test, which is more sensitive than the Kolmogorov-Smirnov (KS) test, to examine the histograms. The results are almost consistent with the KS test, but at different confidence levels for HABs at $z = 0.40$ and OIIbBs at $z = 1.46$. With the AD test, the 95% confidence level that we can reject the null hypothesis for HABs at $z = 0.40$ are higher than that obtained from the KS test, while the null hypothesis for OIIbBs at $z = 1.46$ can be rejected at the 75% confidence level. For OIIbBs at $z = 1.19$, we can still reject the null hypothesis at the same 99% confidence level. From both statistical tests, the blobs with spatially extended $\text{H}\alpha$ or $[\text{O II}]$ emission lines are among those of the most massive emitters at the redshift. It is indicated that large-scale outflows are more prominent in the massive star-forming galaxies.

We plot the difference of specific star formation rate (sSFR) between our sample and the star formation main sequence at $z \sim 1$ by Elbaz et al. (2007) in Figure 13 to compare the star formation activity of blobs with those of the emitters with the same line fluxes. There are a number of HABs with the sSFR lower than a majority of the $\text{H}\alpha$ emitters ($\Delta \log(\text{sSFR}) < 0.0$), suggesting that their star formation activity is relatively more quiescent than most of the star-forming galaxies at the same redshift. Interestingly, while most emitters are located around $\Delta \log(\text{sSFR}) = 0$, a significant number of them show remarkably high sSFR, especially the $[\text{O III}]$ emitters. This suggests that the $[\text{O III}]$ emitters are mostly starbursts. At $z > 1$, the histogram of $[\text{O II}]$ emitters is marginally shifted to $\Delta \log(\text{sSFR})$ greater than zero with 30% of $[\text{O II}]$ emitters at $z = 1.19$ at the highest $\Delta \log(\text{sSFR})$. The blobs at each redshift have the same sSFR distributions as the emitters. According to the AD and the KS tests, we cannot rule out the null hypothesis that they are drawn from the same distribution.

In conclusion, all types of blobs show a variety in star formation activity ranging from the most active star formation like a starburst to quiescent activity. It is implied that the physical mechanism driving the extended emission in the blobs can be individually different from each other. The only property that most blobs have in common is the stellar mass. HABs and OIIbBs are located at the massive end of the distributions of the corresponding normal emitters.

4.3. Cumulative Function of Surface Luminosity Limit

We plot the cumulative number densities of each type of blobs as a function of surface luminosity (SL) limits in Figure 14. The number density at each SL limit is derived by reselecting the blobs with isophotal area above 900 kpc^2 down to different SL limits. As a cumulative number density, the number density at the fainter SL limit, by definition, includes the number of blobs selected by the brighter limit. Therefore, the number density of blobs undoubtedly decreases with increasing the SL limit. Note that the SL limits shown in Figure 14 are corrected for dust extinction by adopting the typical color excess of blobs ($E(B-V) = 0.3 \text{ mag}$) derived by the SED fitting and assuming the equivalent attenuation of the nebular and stellar components. This value is consistent with the extinction correction used in various studies of emitters (e.g., Drake et al. 2013; Sobral et al. 2013).

The top panel of Figure 14 shows cumulative number densities of HABs at $z = 0.25$ and $z = 0.40$. Although we have only an upper limit for the HABs at $z = 0.25$, the number density seems to be smaller than those at $z = 0.40$ if we extrapolate the number density at $z = 0.40$ to the SL limit for

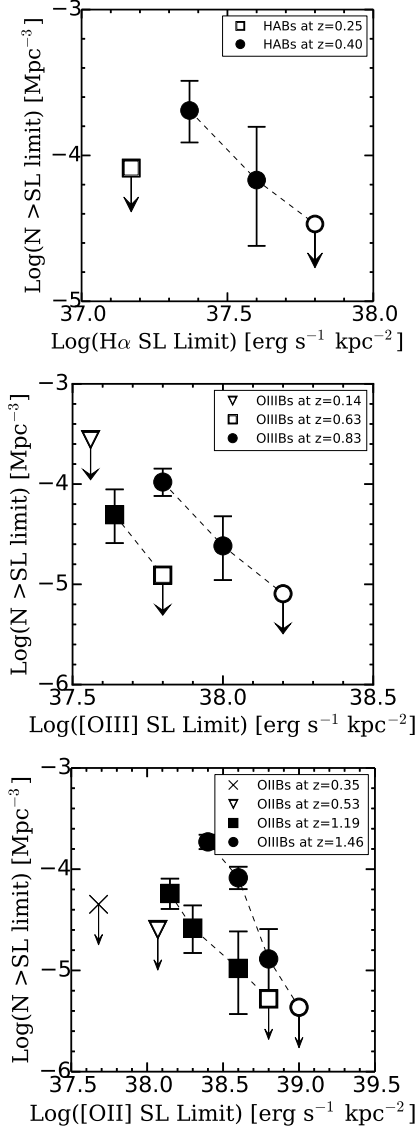


Figure 14. Cumulative number density of the HABs (*top*), O IIIBs (*middle*), and O IIBs (*bottom*) at $z = 0.25 - 1.46$. All blobs are selected with isophotal area larger than 900 kpc^2 measured down to the surface luminosity indicated in the horizontal axis. Open symbols represent the upper limits, while circles, squares, triangles, and crosses indicate the number densities of blobs selected by using the *NB921*, *NB816*, *NB570*, and *NB503* images, respectively.

HABs at $z = 0.25$. (i.e., $H\alpha$ SL limit $\sim 10^{37.2} \text{ erg s}^{-1} \text{ kpc}^{-2}$). Similarly, the number density of the blobs at $z = 0.63$ is lower than the number density of the blobs at $z = 0.83$ at the faintest end as seen in the middle panel of Figure 14. However, the upper limit of the number density of the blobs at $z = 0.14$ is too high to make any conclusive discussion.

The bottom panel of Figure 14 shows the number densities of O IIBs at $z = 0.35 - 1.46$. The number density decreases from $z = 1.46$ to $z = 1.19$ especially at the faint end of surface luminosity limits. Including the upper limits at $z = 0.35$ and $z = 0.53$, the number densities of O IIBs tend to decrease with redshifts. It is seen that the evolution of decreasing number density of blobs as a function of redshifts seems to be common in all types of blobs, though we only observe upper limits at some redshifts.

So far, we investigate the evolution of number densities sep-

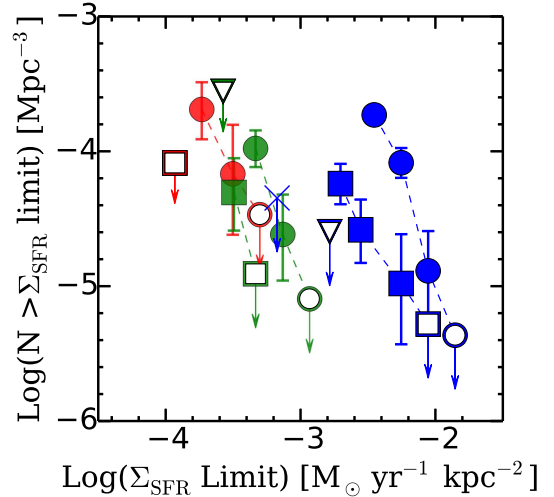


Figure 15. Cumulative number density as a function of surface SFR limit for all types of blobs at $z = 0.25 - 1.46$. Similar to Figure 14, circles, squares, triangles, and crosses represent blobs selected with *NB921*, *NB816*, *NB570*, and *NB503*, respectively. The upper limits of the number densities are shown with open symbols. Red, green, and blue colors indicate the blobs with extended $H\alpha$, [O III], and [O II] emission, respectively.

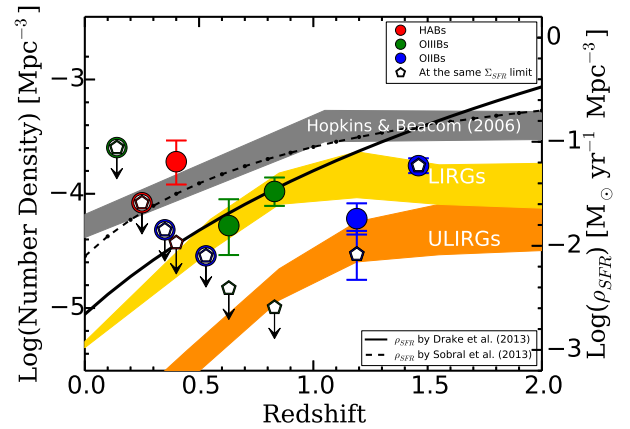


Figure 16. Number densities of HABs (red), O IIIBs (green), and O IIBs (blue) at $z = 0.14 - 1.46$ as a function of redshifts. Circles and pentagons represent the blobs with isophotal area larger than 900 kpc^2 measured down to the flux limit of $1.2 \times 10^{-18} \text{ erg s}^{-1} \text{ cm}^{-2} \text{ arcsec}^{-2}$ and the surface SFR limit of $2.5 \times 10^{-3} M_{\odot} \text{ yr}^{-1} \text{ kpc}^{-2}$, respectively. Downward arrows indicate upper limits in the case of no selected blob. Grey, yellow, and orange contours show the overall star formation rate densities of star-forming galaxies (Hopkins & Beacom 2006), those of LIRGs, and ULIRGs (Casey et al. 2014), respectively. Solid and dashed lines show the star formation rate densities of various emitters at similar redshifts by Drake et al. (2013) and Sobral et al. (2013), respectively.

arately for each type of blobs according to the emission lines we used to select them. We cannot directly compare blobs selected with different emission lines. In order to make a fair comparison across all types of blobs, we convert the surface limit of each emission-line luminosity into the surface SFR (Σ_{SFR}) limit. The $H\alpha$ and [O II] surface luminosities are converted to the surface SFR by using the relations given by Kennicutt (1998). For the [O III] emission line, we adopt the SFR calculation by Drake et al. (2013), which uses the $H\alpha/H\beta$ ratio of 2.78 and [O III]/ $H\beta$ ratio of 3.0 (Osterbrock & Ferland 2006). Although it is simple assumption for the star-forming galaxies, it is well in agreement with the typical line ratios of star-forming galaxies at $z = 0.47 - 0.92$ (Nakajima et al.

2013; Lilly et al. 2003). Figure 15 shows the number densities of all blobs as a function of the Σ_{SFR} limit. It is seen that each type of blobs is located in different ranges of the Σ_{SFR} limit. This is solely due to the fact that each emission line relates to the SFR differently. The Σ_{SFR} limits for the O II B s stand out of the others at high Σ_{SFR} . Comparing within O II B population, we find significant evolution that the number densities of the O II B s tends to decrease with redshifts from $z = 1.46$ to $z = 1.19$. If we naively extrapolate the number densities of O II B s at $z = 1.19 - 1.46$ toward the lower Σ_{SFR} limit, the trend of declining number densities of blobs seems to continue down to $z = 0.83$ (green circles in Figure 15). At lower redshifts, the number densities show slight evolution from $z = 0.83$ to $z = 0.63$ and are comparable at $z < 0.63$, suggesting no significant evolution in that period of the universe.

4.4. Number Density Evolutions of Blobs

In order to obtain a clearer picture of the evolution of blob number densities, we plot the number densities of all blobs selected down to the same flux limit as described in section 2 with filled circles in Figure 16. The star formation rate densities (SFRD) of emitters (Drake et al. 2013; Sobral et al. 2013), star-forming galaxies (Hopkins & Beacom 2006), luminous infrared galaxies (LIRGs), and ultraluminous infrared galaxies (ULIRGs; Casey et al. 2014) are shown to examine if the decrease in number density of blobs is similar to those of other galaxies. As discussed earlier, the number density tends to decrease with decreasing redshifts similar to the SFRD of the emitters, if we consider each type of blob separately. In contrast, the number densities seem to be almost constant within the error bars when comparing them across the types of blobs.

In fact, the blobs that we select with the isophotal area down to the same flux limit cannot be compared across different types of emission lines at different redshifts. We thus re-select all types of blobs with the isophotal area larger than 900 kpc^2 down to the same Σ_{SFR} limit of $2.5 \times 10^{-3} M_{\odot} \text{yr}^{-1} \text{ kpc}^{-1}$ to make a fair comparison among all types of blobs at different redshifts. The resulting number densities are shown with open pentagons in Figure 16. Unfortunately, we only obtain the number densities of blobs at the highest redshifts ($z = 1.19$ and $z = 1.46$), while an upper limit is shown at $z < 1.0$. The number densities of blobs at $z \geq 0.83$ tend to decrease drastically toward lower redshifts. This decrease is even more rapid than the decline of cosmic star formation density, but it seems to be roughly comparable to the decline of ULIRGs. At $z < 0.83$, the upper limits are not useful to interpret as the survey volume is probably too small to draw any conclusion. Larger and deeper survey is desirable to search for blobs with extended emission lines at low redshifts.

As mentioned in Section 1, we develop the method to select the blobs with spatially extended emission lines in order to systematically study the large-scale outflow. The outflow signature in a number of blobs is spectroscopically confirmed (Yuma et al. 2013; Harikane et al. 2014, Yuma et al. in prep.). If we naively consider all blobs as a galactic-scale outflow, we will be able to interpret the evolution of the blobs as that of the outflow events. Therefore, it is implied that the large-scale outflow events decrease significantly with redshifts at more rapid rate than the decline of the cosmic star formation density. The detailed study of the outflow process from blobs will be in the upcoming paper (Yuma et al. in prep.).

5. SUMMARY

Following the first systematic survey of [O II] blobs at $z = 1.19$ by Y13, we expand our search to galaxies with extended [O II] $\lambda\lambda 3726, 3729$, [O III] $\lambda\lambda 4959, 5007$, and $\text{H}\alpha\lambda 6563$ emission lines, which we call O II B, O III B, and HAB, respectively. The redshifts of blob samples range from $z = 0.14$ to $z = 1.46$ covering roughly 9 Gyr of the Universe. We use all narrowband and broadband images available in the SXDS field; i.e., *NB503*, *NB570*, *NB816*, *NB921*, B, V, R, i' , and z' . The blobs are selected with two isophotal area criteria: $> 900 \text{ kpc}^2$ and $> 1500 \text{ kpc}^2$. In this paper, we develop new quantitative approaches to effectively select the blobs with genuine extended emission lines. We simulate the bright PSFs and measure their isophotal area to exclude the bright PSF-like emitters that can mimic the extended feature of the emission lines in the blobs. Furthermore, we create the equivalent-width map to examine if the extended feature of the emission line is real or it is just emission from the neighboring objects. This new method can efficiently exclude the emitters with very close nearby objects and is independent of personal bias, because we do not use visual inspection to determine the extended blobs as done by Y13. Our main results are summarized as follows:

1. With the criterion of isophotal area larger than 900 kpc^2 , we obtain 4 O III B s at $z = 0.63$ and 11 O II B s at $z = 1.19$ selected with the *NB816* image and 6 HABs at $z = 0.40$, 13 O III B s at $z = 0.83$, and 43 O II B s at $z = 1.46$ selected with the *NB921* image.
2. With the larger isophotal-area criterion ($> 1500 \text{ kpc}^2$), we find only one HAB at $z = 0.40$, two O III B s at $z = 0.83$, three O II B s at $z = 1.19$, and six O II B s at $z = 1.46$.
3. We carry out the spectroscopic follow-up observations and confirm that two O III B s are at $z = 0.62 - 0.64$ and the other two are at $z = 0.84$. They all show significant spatial extension of the [O III] emission compared to their stellar components.
4. We check the AGN contribution by using the X-ray and radio catalogs and found few percent of blobs are likely to host an AGN. The fraction of AGNs increases with isophotal area of the emission lines.
5. We make a fair comparison of the stellar properties between the blobs and emitters with the same emission-line fluxes. Histograms of the stellar masses indicate that HABs and O II B s are on average more massive than the normal emitters at the same redshifts. However, we cannot reject the null hypothesis that the distributions of specific SFRs are drawn from the same distributions as the emitters.
6. As a systematic search, we are able to investigate the evolution of number densities of blobs and subsequently the evolution of the large-scale outflow events. Considering each type of the blob separately, we found a decreasing trend of number densities toward lower redshifts in O III B and O II B samples with upper limits at some redshifts at the lowest end. However, if we compare the blobs across the different emission lines, we found no evolution at $z = 0.40 - 0.63$. This comparison is slightly biased, because the same observed flux limit we used to measure the isophotal area corresponds to different luminosity limit at different redshifts.

7. In order to make a fair comparison, we re-select the blobs down to the same surface star formation rate limit. Although the number densities become upper limits for most redshifts, we could at least constrain that the number densities of blobs drastically decrease toward low redshifts. The decreasing trend of the outflow events seems to be steeper than the decline of cosmic star formation density.

For most redshifts, we need deeper and larger imaging surveys to get rid of the upper limits and obtain the better constraint of the evolution of the blobs. The ongoing Hyper Suprime-Cam legacy survey with total 300 nights observed with the Subaru telescope will hopefully provide great number of candidates for blobs with extended emission lines, which are the galaxies with potentially large-scale outflows.

The authors would like to thank an anonymous referee for detailed comments that improved clarity of this article. We also thank Christopher J. Conselice, the ApJ scientific editor, for useful comments on the Anderson-Darling test. This work is supported by Faculty of Science, Mahidol University, Thailand and the Thailand Research Fund (TRF) through research grant for new scholar (MRG5980153). S.Y. thanks David J. Ruffolo for helpful suggestions as a mentor through the TRF research grant. S.Y. acknowledges support from the Japan Society for the Promotion of Science (JSPS) and the Talent Management program at Mahidol University, Thailand. M.O. is supported by World Premier International Research Center Initiative (WPI Initiative), MEXT, Japan, and KAKENHI (15H02064) Grant-in-Aid for Scientific Research (A) through JSPS. A.B.D. acknowledge ANR FOGHAR grant ANR-13-BS05-0010-02. This work is based on data collected at Subaru Telescope, which is operated by the National Astronomical Society of Japan.

REFERENCES

- Aguirre, A., Dow-Hygelund, C., Schaye, J., & Theuns, T. 2008, *ApJ*, 689, 851
- Aird, J., Coil, A. L., Georgakakis, A., Nandra, K., Barro, G., & Pérez-González, P. G. 2015, *MNRAS*, 451, 1892
- Alexander, D. M., Swinbank, A. M., Smail, I., McDermid, R., & Nesvadba, N. P. H. 2010, *MNRAS*, 402, 2211
- Barger, A. J. & Cowie, L. L. 2005, *ApJ*, 635, 115
- Barger, A. J., Cowie, L. L., Mushotzky, R. F., Yang, Y., Wang, W.-H., Steffen, A. T., & Capak, P. 2005, *AJ*, 129, 578
- Benson, A. J., Bower, R. G., Frenk, C. S., et al. 2003, *ApJ*, 599, 38
- Bertin, E. & Arnouts, S. 1996, *A&AS*, 117, 393
- Bradshaw, E. J., Almaini, O., Hartley, W. G., et al. 2013, *MNRAS*
- Bruzual, G. & Charlot, S. 2003, *MNRAS*, 344, 1000
- Calzetti, D., Armus, L., Bohlin, R. C., et al. 2000, *ApJ*, 533, 682
- Casey, C. M., Narayanan, D., & Cooray, A. 2014, *Phys. Rep.*, 541, 45
- Cheung, E., Bundy, K., Cappellari, M., et al. 2016, *Nature*, 533, 504
- Drake, A. B., Simpson, C., Baldry, I. K., et al. 2015, *MNRAS*, 454, 2015
- Drake, A. B., Simpson, C., Collins, C. A., et al. 2013, *MNRAS*, in press
- Elbaz, D., Daddi, E., Le Borgne, D., et al. 2007, *A&A*, 468, 33
- Erb, D. K., Quider, A. M., Henry, A. L., & Martin, C. L. 2012, *ApJ*, 759, 26
- Fotopoulou, S., Buchner, J., Georgantopoulos, I., et al. 2016, *A&A*, 587, A142
- Fumagalli, M., O’Meara, J. M., & Prochaska, J. X. 2011, *Sci*, 334, 1245
- Furusawa, H., Kosugi, G., Akiyama, M., et al. 2008, *ApJS*, 176, 1
- Harikane, Y., Ouchi, M., Yuma, S., et al. 2014, *ApJ*, 794, 129
- Heckman, T. M., Armus, L., & Miley, G. K. 1990, *ApJS*, 74, 833
- Hopkins, A. M. & Beacom, J. F. 2006, *ApJ*, 651, 142
- Jansen, F., Lumb, D., Altieri, B., et al. 2001, *A&A*, 365, L1
- Kashikawa, N., Aoki, K., Asai, R., et al. 2002, *PASJ*, 54, 819
- Kennicutt, Jr., R. C. 1998, *ARA&A*, 36, 189
- Kewley, L. J., Maier, C., Yabe, K., et al. 2013, *ApJL*, 774, L10
- Kornei, K. A., Shapley, A. E., Martin, C. L., Coil, A. L., Lotz, J. M., Schiminovich, D., Bundy, K., & Noeske, K. G. 2012, *ApJ*, 758, 135
- Lamareille, F. 2010, *A&A*, 509, A53
- Lamareille, F., Mouhcine, M., Contini, T., Lewis, I., & Maddox, S. 2004, *MNRAS*, 350, 396
- Lawrence, A., Warren, S. J., Almaini, O., et al. 2007, *MNRAS*, 379, 1599
- Lilly, S. J., Carollo, C. M., Pipino, A., Renzini, A., & Peng, Y. 2013, *ApJ*, 772, 119
- Lilly, S. J., Carollo, C. M., & Stockton, A. N. 2003, *ApJ*, 597, 730
- Lin, L., Lin, J.-H., Hsu, C.-H., et al. 2017, *arXiv:1702.02464*
- Martin, C. L. 2005, *ApJ*, 621, 227
- Martin, C. L., Shapley, A. E., Coil, A. L., Kornei, K. A., Bundy, K., Weiner, B. J., Noeske, K. G., & Schiminovich, D. 2012, *ApJ*, 760, 127
- McIntosh, D. H., Bell, E. F., Rix, H.-W., et al. 2005, *ApJ*, 632, 191
- Nakajima, K. & Ouchi, M. 2014, *MNRAS*, 442, 900
- Nakajima, K., Ouchi, M., Shimasaku, K., et al. 2013, *ApJ*, 769, 3
- Nesvadba, N. P. H., Lehnert, M. D., De Breuck, C., Gilbert, A. M., & van Breugel, W. 2008, *A&A*, 491, 407
- Oke, J. B. & Gunn, J. E. 1983, *ApJ*, 266, 713
- Osterbrock, D. E. & Ferland, G. J. 2006 (Mill Valley, CA), 40
- Ouchi, M., Ono, Y., Egami, E., et al. 2009, *ApJ*, 696, 1164
- Ouchi, M., Shimasaku, K., Akiyama, M., et al. 2008, *ApJS*, 176, 301
- Overzier, R. A., Heckman, T. M., Tremonti, C., et al. 2009, *ApJ*, 706, 203
- Ranalli, P., Koulouridis, E., Georgantopoulos, I., et al. 2016, *A&A*, 590, A80
- Salpeter, E. E. 1955, *ApJ*, 121, 161
- Sawicki, M. 2012, *PASP*, 124, 1208
- Schawinski, K., Koss, M., Berney, S., & Sartori, L. F. 2015, *MNRAS*, 451, 2517
- Simpson, C., Martínez-Sansigre, A., Rawlings, S., et al. 2006, *MNRAS*, 372, 741
- Simpson, C., Rawlings, S., Ivison, R., et al. 2012, *MNRAS*, 421, 3060
- Sobral, D., Smail, I., Best, P. N., Geach, J. E., Matsuda, Y., Stott, J. P., Cirasuolo, M., & Kurk, J. 2013, *MNRAS*, 428, 1128
- Somerville, R. S., Hopkins, P. F., Cox, T. J., Robertson, B. E., & Hernquist, L. 2008, *MNRAS*, 391, 481
- Soto, K. T., Martin, C. L., Prescott, M. K. M., & Armus, L. 2012, *ApJ*, 757, 86
- Steidel, C. C., Erb, D. K., Shapley, A. E., Pettini, M., Reddy, N., Bogosavljević, M., Rudie, G. C., & Rakic, O. 2010, *ApJ*, 717, 289
- Strüder, L., Briel, U., Dennerl, K., et al. 2001, *A&A*, 365, L18
- Trujillo, I. & Aguerri, J. A. L. 2004, *MNRAS*, 355, 82
- Turner, M. J. L., Abbey, A., Arnaud, M., et al. 2001, *A&A*, 365, L27
- Ueda, Y., Watson, M. G., Stewart, I. M., et al. 2008, *ApJS*, 179, 124
- Walter, F., Weiss, A., & Scoville, N. 2002, *ApJL*, 580, L21
- Yuma, S., Ouchi, M., Drake, A. B., et al. 2013, *ApJ*, 779, 53

APPENDIX

Catalogs of all blobs at $z = 0.40 - 1.46$ are listed below. It is noteworthy that the observed flux and luminosity of the emission lines listed here are not corrected for the dust extinction yet.

Table A1
Catalog of HABs at $z = 0.40$ in the SXDS field

Object Name ^a	α (J2000)	δ (J2000)	$NB921-z'$ ^b (mag)	$F(H\alpha)$ (10^{-16} erg s $^{-1}$ cm $^{-2}$)	$L(H\alpha)$ (10^{41} erg s $^{-1}$)	Isophotal Area (arcsec 2)
Isophotal area more than 1500 kpc 2						
HAB040m-1	02 16 11.787	-04 45 16.952	20.39 ± 0.09	11.8 ± 1.1	6.7 ± 0.6	54
Isophotal area more than 900 kpc 2						
HAB040s-2	02 17 21.392	-04 43 02.577	20.78 ± 0.12	8.3 ± 1.0	4.7 ± 0.6	45
HAB040m-3	02 17 24.184	-05 25 26.949	20.67 ± 0.11	9.2 ± 1.1	5.2 ± 0.6	40
HAB040m-4	02 17 23.373	-05 13 53.316	21.34 ± 0.13	5.0 ± 0.6	2.8 ± 0.3	37
HAB040m-5	02 17 03.259	-05 24 23.957	20.67 ± 0.12	9.1 ± 1.1	5.2 ± 0.6	35
HAB040m-6	02 18 59.135	-05 23 37.375	21.24 ± 0.14	5.4 ± 0.8	3.1 ± 0.4	33

^a The letters "m" and "s" after HAB040 mean "multiple" and "single", respectively. They are used to indicate the number of continuum components of the blobs.

^b $NB921-z'$ magnitudes are measured down to 1.2×10^{-18} erg s $^{-1}$ cm $^{-2}$ arcsec $^{-2}$.

Table A2
Catalog of O IIIBs at $z = 0.63$ in the SXDS field

Object Name	α (J2000)	δ (J2000)	$NB816-Rz$ ^a (mag)	$F([O III])$ (10^{-16} erg s $^{-1}$ cm $^{-2}$)	$L([O III])$ (10^{41} erg s $^{-1}$)	Isophotal Area (arcsec 2)
Isophotal area more than 900 kpc 2						
OIIIB063s-1	02 17 50.244	-05 00 04.159	22.04 ± 0.14	3.0 ± 0.4	4.99 ± 0.7	24
OIIIB063s-2	02 19 05.902	-05 13 48.599	22.27 ± 0.15	2.4 ± 0.4	4.04 ± 0.7	24
OIIIB063s-3	02 18 31.564	-05 24 24.611	22.12 ± 0.15	2.8 ± 0.4	4.65 ± 0.7	23
OIIIB063s-4	02 17 09.652	-04 44 16.176	21.71 ± 0.15	4.0 ± 0.6	6.76 ± 1.0	22

Note: There is no O IIIb at $z = 0.63$ with the isophotal area larger than 1500 kpc 2 and all O IIIBs at this redshift have only one stellar component.

^a $NB816-Rz$ magnitudes are measured down to 1.2×10^{-18} erg s $^{-1}$ cm $^{-2}$ arcsec $^{-2}$.

Table A3
Catalog of O IIIBs at $z = 0.83$ in the SXDS field

Object Name ^a	α (J2000)	δ (J2000)	$NB921-z'$ ^b (mag)	$F([O III])$ (10^{-16} erg s $^{-1}$ cm $^{-2}$)	$L([O III])$ (10^{41} erg s $^{-1}$)	Isophotal Area (arcsec 2)
Isophotal area more than 1500 kpc 2						
OIIIB083m-1	02 18 58.757	-05 16 57.162	21.89 ± 0.11	3.0 ± 0.3	9.8 ± 1.0	35
OIIIB083m-2	02 19 03.734	-05 11 53.243	22.77 ± 0.13	1.3 ± 0.2	4.4 ± 0.6	29
Isophotal area more than 900 kpc 2						
OIIIB083m-3	02 19 03.780	-05 28 53.328	22.05 ± 0.18	2.6 ± 0.5	8.48 ± 1.5	21
OIIIB083m-4	02 19 06.479	-05 10 57.034	23.55 ± 0.21	0.6 ± 0.1	2.14 ± 0.3	20
OIIIB083m-5	02 18 13.016	-04 48 48.277	23.52 ± 0.22	0.7 ± 0.2	2.18 ± 0.6	19
OIIIB083s-6	02 18 05.812	-04 40 15.911	22.44 ± 0.21	1.8 ± 0.4	5.94 ± 1.2	19
OIIIB083m-7	02 18 27.313	-05 17 42.059	22.08 ± 0.20	2.5 ± 0.5	8.25 ± 1.5	19
OIIIB083m-8	02 18 47.713	-05 24 35.981	22.59 ± 0.23	1.6 ± 0.4	5.15 ± 1.2	19
OIIIB083s-9	02 18 54.318	-04 47 34.030	22.49 ± 0.22	1.7 ± 0.4	5.68 ± 1.2	18
OIIIB083s-10	02 17 46.527	-04 44 13.844	23.20 ± 0.23	0.9 ± 0.2	2.94 ± 0.6	18
OIIIB083m-11	02 17 56.121	-04 46 09.748	21.95 ± 0.22	2.8 ± 0.6	9.29 ± 1.8	17
OIIIB083m-12	02 18 58.701	-05 12 58.126	23.32 ± 0.23	0.8 ± 0.2	2.64 ± 0.6	17
OIIIB083s-13	02 19 03.915	-04 46 57.229	23.16 ± 0.25	0.9 ± 0.2	3.06 ± 0.6	16

^a The letters "m" and "s" after OIIIB083 mean "multiple" and "single", respectively. They are used to indicate the number of continuum components of the blobs.

^b $NB921-z'$ magnitudes are measured down to 1.2×10^{-18} erg s $^{-1}$ cm $^{-2}$ arcsec $^{-2}$.

Table A4
Catalog of O II Bz at $z = 1.19$ in the SXDS field

Object Name ^a	α (J2000)	δ (J2000)	$NB816-Rz^b$ (mag)	$F([O II])$ (10^{-16} erg s $^{-1}$ cm $^{-2}$)	$L([O II])$ (10^{41} erg s $^{-1}$)	Isophotal Area (arcsec 2)
Isophotal area more than 1500 kpc 2						
OIIB119m-1	02 17 08.642	-04 50 22.876	22.01 ± 0.10	3.1 ± 0.3	24.6 ± 2.4	34
OIIB119m-2	02 17 16.345	-04 57 11.938	21.78 ± 0.11	3.8 ± 0.4	3.03 ± 3.2	31
OIIB119m-3	02 18 55.226	-05 21 17.681	23.30 ± 0.15	0.9 ± 0.1	7.5 ± 0.8	26
Isophotal area more than 900 kpc 2						
OIIB119m-4	02 19 19.090	-05 15 35.280	22.77 ± 0.17	1.5 ± 0.2	12.2 ± 1.6	21
OIIB119m-5	02 17 34.407	-04 58 59.858	23.40 ± 0.18	0.9 ± 0.2	6.8 ± 1.6	20
OIIB119s-6	02 19 01.684	-04 59 33.233	23.68 ± 0.21	0.7 ± 0.1	5.3 ± 0.8	18
OIIB119s-7	02 18 56.110	-04 45 50.865	23.23 ± 0.20	0.9 ± 0.2	8.0 ± 1.6	17
OIIB119s-8	02 17 45.842	-04 42 40.343	23.16 ± 0.20	1.1 ± 0.2	8.5 ± 1.6	17
OIIB119m-9	02 18 59.747	-04 49 41.717	23.68 ± 0.24	0.7 ± 0.2	5.3 ± 1.6	16
OIIB119s-10	02 18 53.660	-05 15 23.773	23.87 ± 0.26	0.6 ± 0.2	4.5 ± 1.6	14
OIIB119s-11	02 17 32.526	-04 57 46.401	22.90 ± 0.25	1.4 ± 0.3	10.8 ± 2.4	14

^a The letters "m" and "s" after OIIB119 mean "multiple" and "single", respectively. They are used to indicate the number of continuum components of the blobs.

^b $NB816-Rz$ magnitudes are measured down to 1.2×10^{-18} erg s $^{-1}$ cm $^{-2}$ arcsec $^{-2}$.

Table A5
Catalog of O IIbBs at $z = 1.46$ in the SXDS field

Object Name ^a	α (J2000)	δ (J2000)	$NB921-z'$ ^b (mag)	$F([\text{O II}])$ (10^{-16} erg s $^{-1}$ cm $^{-2}$)	$L([\text{O II}])$ (10^{41} erg s $^{-1}$)	Isophotal Area (arcsec 2)
Isophotal area more than 1500 kpc 2						
OIIb146m-1	02 19 6.034	-05 03 35.552	22.50 \pm 0.13	1.7 \pm 0.2	22.6 \pm 2.7	36
OIIb146s-2	02 16 50.983	-05 01 37.451	22.64 \pm 0.13	1.5 \pm 0.2	19.9 \pm 2.7	28
OIIb146m-3	02 17 04.783	-05 15 18.450	22.72 \pm 0.17	1.4 \pm 0.2	18.5 \pm 2.7	28
OIIb146m-4	02 19 06.426	-04 57 55.386	22.45 \pm 0.15	1.8 \pm 0.3	23.8 \pm 4.0	26
OIIb146m-5	02 17 47.428	-05 12 59.786	22.96 \pm 0.16	1.1 \pm 0.2	14.9 \pm 2.7	25
OIIb146m-6	02 17 00.352	-05 01 50.586	22.94 \pm 0.19	1.1 \pm 0.2	15.1 \pm 2.7	22
Isophotal area more than 900 kpc 2						
OIIb146s-7	02 19 04.834	-04 54 14.670	23.45 \pm 0.20	0.7 \pm 0.1	9.45 \pm 1.3	21
OIIb146s-8	02 19 02.692	-04 47 23.322	23.01 \pm 0.19	1.06 \pm 0.2	14.1 \pm 2.7	21
OIIb146m-9	02 17 23.563	-05 05 40.962	23.26 \pm 0.20	0.8 \pm 0.2	11.3 \pm 2.7	21
OIIb146m-10	02 18 26.308	-05 12 57.343	23.06 \pm 0.19	1.01 \pm 0.2	13.5 \pm 2.7	21
OIIb146m-11	02 18 26.206	-05 12 56.843	23.06 \pm 0.19	1.01 \pm 0.2	13.5 \pm 2.7	21
OIIb146s-12	02 18 12.194	-05 01 11.636	22.45 \pm 0.19	1.77 \pm 0.3	23.6 \pm 4.0	20
OIIb146m-13	02 18 50.247	-05 00 46.797	22.64 \pm 0.21	1.50 \pm 0.3	19.9 \pm 4.0	20
OIIb146m-14	02 17 13.236	-05 21 41.889	23.30 \pm 0.21	0.8 \pm 0.2	10.8e \pm 2.7+42	20
OIIb146m-15	02 17 13.626	-05 09 39.486	23.21 \pm 0.21	0.8 \pm 0.2	11.8 \pm 2.7	20
OIIb146s-16	02 16 58.166	-05 13 39.015	22.68 \pm 0.22	1.44 \pm 0.3	19.2 \pm 4.0	20
OIIb146m-17	02 19 18.176	-04 47 31.143	22.10 \pm 0.19	2.45 \pm 0.4	32.7 \pm 5.3	20
OIIb146s-18	02 19 17.159	-04 52 10.298	22.73 \pm 0.21	1.38 \pm 0.3	18.3 \pm 4.0	19
OIIb146m-19	02 17 34.183	-05 10 16.175	22.22 \pm 0.20	2.19 \pm 0.4	29.2 \pm 5.3	19
OIIb146s-20	02 17 49.028	-05 21 38.785	23.32 \pm 0.21	0.8 \pm 0.2	10.7 \pm 2.7	19
OIIb146m-21	02 17 38.914	-05 12 36.599	22.86 \pm 0.22	1.23 \pm 0.3	16.3 \pm 4.0	19
OIIb146m-22	02 18 17.559	-05 03 58.961	22.51 \pm 0.21	1.69 \pm 0.3	22.5 \pm 4.0	19
OIIb146m-23	02 18 53.618	-05 12 13.477	22.60 \pm 0.21	1.55 \pm 0.3	20.7 \pm 4.0	19
OIIb146s-24	02 18 58.056	-05 21 37.365	23.26 \pm 0.21	0.8 \pm 0.2	11.3 \pm 2.7	19
OIIb146m-25	02 17 09.097	-04 50 47.034	22.76 \pm 0.23	1.34 \pm 0.3	17.8 \pm 4.0	19
OIIb146m-26	02 17 05.657	-04 55 47.036	22.61 \pm 0.21	1.54 \pm 0.3	20.5 \pm 4.0	18
OIIb146m-27	02 17 12.991	-04 54 40.741	22.47 \pm 0.21	1.76 \pm 0.4	23.4 \pm 5.3	18
OIIb146m-28	02 18 56.884	-05 00 56.060	23.82 \pm 0.25	0.5 \pm 0.1	6.70 \pm 1.3	18
OIIb146m-29	02 17 07.843	-04 50 00.902	22.71 \pm 0.23	1.40 \pm 0.3	18.6 \pm 4.0	18
OIIb146s-30	02 17 01.233	-05 28 43.889	23.56 \pm 0.24	0.6 \pm 0.1	8.54 \pm 1.3	17
OIIb146m-31	02 18 26.263	-04 40 55.116	22.81 \pm 0.23	1.27 \pm 0.3	17.0 \pm 4.0	17
OIIb146m-32	02 17 58.677	-05 12 42.674	23.41 \pm 0.24	0.7 \pm 0.2	9.84 \pm 2.7	17
OIIb146m-33	02 17 28.558	-05 13 45.305	22.56 \pm 0.24	1.61 \pm 0.4	21.4 \pm 5.3	16
OIIb146m-34	02 17 13.757	-05 00 01.130	22.74 \pm 0.25	1.36 \pm 0.3	18.1 \pm 4.0	16
OIIb146m-35	02 17 20.349	-04 43 53.291	23.40 \pm 0.25	0.7 \pm 0.2	9.85 \pm 2.7	16
OIIb146m-36	02 17 12.632	-04 54 43.034	23.42 \pm 0.25	0.7 \pm 0.2	9.71 \pm 2.7	16
OIIb146m-37	02 17 14.949	-05 05 28.282	23.09 \pm 0.25	1.0 \pm 0.2	13.1 \pm 2.7	15
OIIb146s-38	02 19 12.393	-05 13 17.377	23.47 \pm 0.27	0.7 \pm 0.2	9.30 \pm 2.7	15
OIIb146m-39	02 17 47.709	-05 23 07.385	23.34 \pm 0.28	0.7 \pm 0.2	10.5 \pm 2.7	14
OIIb146s-40	02 18 30.241	-05 04 10.890	22.97 \pm 0.28	1.10 \pm 0.3	14.7 \pm 4.0	14
OIIb146m-41	02 19 04.278	-05 19 59.379	23.61 \pm 0.31	0.6 \pm 0.2	8.17 \pm 2.7	13
OIIb146m-42	02 18 34.744	-05 03 00.816	22.73 \pm 0.30	1.38 \pm 0.4	18.4 \pm 5.3	13
OIIb146m-43	02 17 47.512	-05 10 53.431	23.42 \pm 0.29	0.7 \pm 0.2	9.67 \pm 2.7	13

^a The letters "m" and "s" after OIIb146 mean "multiple" and "single", respectively. They are used to indicate the number of continuum components of the blobs.

^b $NB921-z'$ magnitudes are measured down to 1.2×10^{-18} erg s $^{-1}$ cm $^{-2}$ arcsec $^{-2}$.